Correspondence: Dr. Alan M. Jones
Address: Department of Biology
The University of North Carolina at Chapel Hill
Coker Hall, CB#3280

Phone : (919) 962-6932
Fax: (919) 962-1625
E-mail: alan_jones@unc.edu

The author responsible for distribution of materials integral to the findings presented in this article is Dr. Alan Jones alan_jones@unc.edu

Running Title: Biased System Signaling

Keywords:

Title: Biased Signaling: Distinct Ligand-directed Plasma Membrane Signalosomes Using a Common RGS/ G protein Core

AUTHORS **Timothy J. Ross-Elliott[1], Justin Watkins[1], Xiaoyi Shan[2], Fei Lou[1], Bernd Dreyer[1], Meral Tunc-Ozdemir[1], Haiyan Jia[1], Jing Yang[1], Luguang Wu[2], Yuri Trusov[3], Patrick Krysan[4], and Alan M. Jones[1, 3, 5]**

Department of [1] Biology and [3] Pharmacology, University of North Carolina at Chapel Hill, Chapel Hill, NC 27599, USA.

[2]Beijing Forestry University, Beijing China 1000083

[3]School of Agriculture and Food Science, The University of Queensland, St. Lucia, Q4072, Australia.

[4]Department of Horticulture, University of Wisconsin Madison, Madison, WI 53706, USA

[5]Lead Contact

*Correspondence: alan_jones@unc.edu

Keywords: Arrestin analog, AtRGS1, calcium signaling, clathrin-mediated endocytosis, MAPK activation, proximity labeling, sterol-dependent endocytosis, VPS26, WNK kinase,

Abbreviations: *Arabidopsis thaliana* Regulator of G Signaling (AtRGS1), Clathrin-Mediated Endocytosis (CME), Sterol-Dependent Endocytosis (SDE), Total Internal Reflection Fluorescence Microscopy (TIRF), Clathrin Light Chain (CLC), Flotilin 1 (FLOT1), Vacuolar Protein Sorting 26 (VPS26)

SUMMARY

Biased signaling occurs when different ligands that are directed at the same receptor launch different cellular outcomes. Because of their pharmacological importance, we know the most about biased ligands and little is known about other mechanisms to achieve signaling bias. In the canonical animal G protein system, endocytosis of a 7-transmembrane GPCR desensitizes a cell from an extracellular signal. β-arrestins facilitate GPCR endocytosis but also propagates cytoplasmic signaling depending on the bias. In Arabidopsis, GPCRs are not required for G protein coupled signaling because the heterotrimeric G protein complex spontaneously exchanges nucleotide. Instead, the prototype 7-transmembrane Regulator of G Signaling 1 protein AtRGS1 modulates G signaling and through ligand-dependent endocytosis, de-repression of signaling is initiated but canonical arrestins are not involved. Endocytosis initiates from two separate pools of plasma membrane: microdomains and a clathrin-accessible neighborhood, each with a select set of discriminators, activators, and newly-discovered arrestin-like adaptors. Different trafficking origins and trajectories lead to different cellular outcomes. Thus, compartmentation with its attendant signalosome architecture is a previously unknown mechanism to drive biased signaling.

INTRODUCTION

Different ligands discriminated by the same receptor or utilizing the same core of signaling elements can set in motion a cascade of events that lead to multiple outcomes. When subsets of outcomes are ligand-specific, we label this biased signaling. This bias can be encoded in the ligand structure (biased ligands), in the receptors (biased receptors), or in the interactions between the signaling components (biased systems) (Smith et al., 2018). Of the three defined mechanisms,

biased ligands is the most widely studied because of its immediate pharmacological significance, such as the development of drugs that provide analgesia without the addictive side effect (Manglik et al., 2016; White et al., 2015; Wingler et al., 2019). **a)** Ligand bias occurs when a ligand stabilizes one or few of several conformations of a receptor protein which then preferentially recruits or activates signaling elements such as arrestin and the heterotrimeric G protein complex that lead toward one cellular outcome over another (Bohn et al., 2000; DeWire et al., 2013). For example, some ligands are biased towards arrestin signaling (Charest et al., 2007; Gesty-Palmer et al., 2006; Shenoy et al., 2006) such as certain dopamine agonists compared to dopamine which is biased towards D_2R-β-arrestin coupling (Allen et al., 2011). Certain opioid agonists compared to morphine are biased toward G-protein signaling (DeWire et al., 2013; Rives et al., 2012; White et al., 2015). **b)** Receptor bias occurs through recognition of the same ligand by multiple receptor types (Géhin et al., 1999) including so-called decoy receptors (Lin and Hsieh, 2011; Pan et al., 1997), some of which may in fact be functional receptors that use non-classical signaling pathways (Lin and Hsieh, 2011; Rajagopal et al., 2010a). Dopamine D_1 and D_2 class receptors recognize dopamine, but signal through different subunits of Gα as well as arrestin (Urs et al., 2017). **c)** System bias involves a cell-mediated shift to one pathway over another by some unknown mechanism but one possibility is through mass action, for example, making arrestin more abundant at the receptor than Gα or a particular kinase (Urs et al., 2016). This last category of bias signaling is the least understood and the subject of the present work.

Phosphorylation patterns are the chemical bar codes for biased signaling at least for arrestin-dependent outcomes (Butcher et al., 2011; Nobles et al., 2011; Shiraishi et al., 2018; Yang et al., 2015; Yang et al., 2017). G-protein coupled Receptor Kinases (GRKs) phosphorylate the C-terminus or other cytoplasmic elements of GPCRs in response to agonist binding, unlike Protein

Kinase A and C that phosphorylate GPCRs in a heterologous manner (Benovic et al., 1986; Sibley et al., 1987). The subsequent coupling of arrestin to phosphorylated GPCRs does not end G-protein independent signaling. Arrestin-bound GPCRs further activates multiple kinase pathways including MAPK and tyrosine kinases (DeFea et al., 2000; Luttrell et al., 2001; Rajagopal et al., 2010b). While plants lack GRK's, an Arabidopsis family of kinases called WITH NO LYSINE (**WNK**) Kinase phosphorylate the C-terminal tail of the non-canonical 7-transmembrane Regulator of G Signaling (**AtRGS1**) in response to extracellular glucose (Fu et al., 2014a; Urano et al., 2012a). AtRGS1 is also phosphorylated by other kinases including BAK1, a co-receptor for flg22 which is a Pathogen-Associated Molecular Pattern (PAMP) (Liang et al., 2018; Tunc-Ozdemir et al., 2017; Tunc-Ozdemir et al., 2016) and loss of AtRGS1 and other G protein components severely affect resistance in a wide range of pathogens (Zhong et al., 2018). System-biased signaling may be particularly relevant in plants where AtRGS1 modulates intracellular signaling transduction through G protein activation. AtRGS1 regulates G protein activation with ligand discrimination likely facilitated by membrane bound Receptor Like Kinases (RLK's) of which there are more than 600 members in Arabidopsis (Shiu and Bleecker, 2001).

In animals, activation of G Protein signaling results from GDP exchange for GTP on the Gα subunit and subsequent dissociation from the GPCR, wherein this nucleotide exchange is the rate-limiting step (Ferguson et al., 1986). Desensitization of the cell toward the signal occurs through endocytosis of the GPCR mediated by arrestins (Benovic et al., 1987; Lohse et al., 1990). In Arabidopsis, however, the Gα subunit, AtGPA1 spontaneously exchanges nucleotide without a GPCR thus it is self-activating and it is the intrinsic GTPase activity that is the rate-limiting step (Johnston et al., 2007; Jones et al., 2011a). AtRGS1 accelerates the intrinsic GTPase of AtGPA1 (Jones et al., 2011b) and as a result, inactive Gα remains bound to GDP until de-repression through

AtRGS1 endocytosis, permitting Gα activation through nucleotide exchange and subsequent downstream signal transduction (Urano et al., 2012a). This AtRGS1 endocytosis is a well-established proxy for sustained G protein activation and the proportion of endocytosed AtRGS1 is linearly related to the proportion of G protein activation (Fu et al., 2014a). In Arabidopsis, sugars (Fu et al., 2014a; Grigston et al., 2008) and flg22 (Tunc-Ozdemir et al., 2016) activate AtRGS1 (Urano et al., 2012b).

Physically de-coupling AtRGS1 from the heterotrimeric G protein complex by endocytosis is the crux of the de-repression mechanism, at least for sustained activation. Two modes of endocytosis in plants are known: Clathrin-Mediated Endocytosis (**CME**) and Sterol-Dependent Endocytosis (**SDE**) (Fan et al., 2015), however, the protein that directly couples to AtRGS1 and is responsible for endocytosis (equivalent of arrestin-2 or -3 for GPCRs in animals) is unknown. Extensive work has been done to elucidate the CME pathway in animal and yeast systems with the function of many molecular components being well characterized. Of particular interest is the ADAPTOR PROTEIN COMPLEX-2 (**AP-2**) that is required for recognition and binding of cargo (Jackson et al., 2010; Kelly et al., 2008; Krauss et al., 2006a), recruiting clathrin to the PM, and the subsequent formation of clathrin-coated vesicles. In the absence of AP-2 function, clathrin-coated vesicle formation is reduced and endocytosis is inhibited (Boucrot et al., 2010). The AP-2 complex is a heteromeric complex consisting of 2 large subunits (α2 and β2), 1 medium subunit (μ2), and 1 small subunit (σ2) (Collins et al., 2002).

SDE is a clathrin-independent mechanism for internalization of membrane-associated proteins. Also referred to as lipid raft endocytosis, SDE of these microdomains requires Flotilin1 (**Flot1**), and possibly the microdomain associated Remorin protein (Raffaele et al., 2009) for internalization of sterol-rich vesicles (Li et al., 2012b). Membrane proteins PIP2;1 and Respiratory

Burst Oxidase Homolog D (**RbohD**) are selectively internalized via sterol-dependent endocytosis under salt stress conditions (Hao et al., 2014; Li et al., 2011).

We present data illustrating a biased system where two distinct extracellular ligands induce endocytosis of AtRGS1 from separate plasma membrane origins, of which one is mediated by a previously-undiscovered plant arrestin-like protein, Vacuolar Protein Sorting 26 (VPS26). flg22 initiates AtRGS1 endocytosis via CME, while glucose activates both pathways of endocytosis. Phosphorylation of AtRGS1 and involvement of individual subunits of the heterotrimeric G protein complex are also ligand specific as are the immediate downstream consequences. From the CME-mediated-AtRGS1 origin, flg22 induces a MAPK cascade known to drive transcriptional reprogramming (Lee et al., 2015), whereas from the SDE-mediated-AtRGS1 origin, glucose induces transcriptional change that is independent of the MAPK cascade.

RESULTS

Biased Signaling by Two Extracellular Signals

To date, there are 2 well-studied signals that directly and rapidly activate the Arabidopsis heterotrimeric G protein signaling pathway through AtRGS1 endocytosis: **1)** flg22 which is a 22-amino acid PAMP from the plant pathogen *Pseudomonas syringe* that is recognized on plant cells to initiate the innate immunity pathway (Asai et al., 2002; Felix et al., 1999; Gómez-Gómez and Boller, 2000). It is already established that flg22 is perceived extracellularly (e.g. (Jelenska et al., 2017) by co-receptors BAK1 and FLS2 as part of a larger G protein complex (Sun et al., 2013; Tunc-Ozdemir and Jones, 2017). **2)**. Glucose or a glucose metabolite which is a product of photosynthesis (Tunc-Ozdemir et al., 2018) and metabolism of starch stores (Pharr and Keller, 2017). An AtRGS1-mediated extracellular site of perception of glucose or its metabolite has not yet been shown.

Many sugars, although primarily sucrose, are transported extracellularly in the apoplastic space where they are converted to glucose by cell wall localized invertases and potentially further metabolized to a signal. These sugars are rapidly taken up through a large family of transporters (Chen et al., 2010; Williams et al., 2000) where they are detected in the cytoplasm, but some sugars may also be detected extracellularly (Li and Sheen, 2016). D-glucose or its metabolite induces rapid endocytosis of AtRGS1-dependent sugar signaling (Fu et al., 2014a; Urano et al., 2012a) and because AtRGS1 shares the membrane topology of GPCRs that perceive extracellular signals, it has been assumed that the extracellular glucose or metabolite is perceived by the AtRGS1/G protein complex. However, neither an extracellular site for perception nor direct evidence for agonist binding to AtRGS1 has been shown. To address the former, impermeant sugars were tested for the ability to activate G signaling.

The glucose-fructose dissacharide 6-0-α-D-glucopyranosyl-D-fructose (aka isomaltulose, pallatinose), is presumed not to be transported across the plant cell membrane although it acts as an active glucose precursor if synthesized intracellularly (Loreti et al., 2000; Sinha et al., 2002). While the expression of sucrose isomerase in potato increased apoplastic isomaltulose, transport across any membrane has yet to be demonstrated (Börnke et al., 2002). Importantly, isomaltulose is not hydrolyzed extracellularly (Fernie et al., 2001; Wu and Birch, 2011). To determine if isomaltulose is impermeant to the plasma membrane, we chemically synthesized [^{14}C] isomaltulose (Figure S1A) and tested for uptake into Arabidopsis seedlings. Isomaltulose was at least 9-fold less permeant to cells than glucose (Figure S1B). Therefore, to determine if sugars are perceived extracellularly by hypocotyl cells, we tested the effect of isomaltulose on AtRGS1-YFP endocytosis (Figure 1A) as a validated proxy for activation of G signaling as previously shown (Fu et al., 2014a; Urano et al., 2012a). Whereas several mono and disaccharides failed to activate

G signaling, extracellular isomaltulose caused AtRGS1 internalization statistically ($P < 0.01$) more effectively than D-glucose (Figure 1B) despite being transported ~10-fold less suggesting that isomaltulose activates AtRGS1 extracellularly. Turanose is another disaccharide that is thought to be perceived extracellularly (Loreti et al., 2000) and is impermeant (Rolland et al., 2002) therefore endpoint analysis was performed using this sugar, and just as for both glucose and isomaltulose, turanose activated G signaling (Figure 1C). Isomaltulose and turanose are disaccharides that share a glucose ring (Figure 1D), suggesting that glucose or a glucose metabolite is the discriminated signal or is important for a metabolic agonist (e.g. sugar nucleotides).

AtRGS1 Endocytic Pathway is Signal Biased

Having shown that extracellular flg22 is detected by BAK1/FLS2 (Chinchilla et al., 2006; Gómez-Gómez and Boller, 2000; Tunc-Ozdemir et al., 2016) and induces AtRGS1 endocytosis (Tunc-Ozdemir et al., 2016) and that extracellular D-glucose acts upstream of AtRGS1 endocytosis, both requiring at least in part the phosphorylation of AtRGS1 at its C terminal tail (Tunc-Ozdemir et al., 2016; Urano et al., 2012a), we turned to the question of whether these two signals activate the same pool of AtRGS1. Endocytosis in plants utilizes two primary pathways: CME and SDE. Both pathways have been individually associated with the activity of specific proteins and responses (Adam et al., 2012; Dhonukshe et al., 2007; Irani et al., 2012; Li et al., 2012b); for example, CME and SDE cooperatively regulate the activity of RbohD in the flg22 pathway (Hao et al., 2014). We used super resolution microscopies to achieve the needed spatial and temporal resolution to answer quantitative differences in signal-induced activation. To determine if one or both pathways regulate AtRGS1 activity at the membrane, we induced internalization with D-glucose and *flg22* while simultaneously inhibiting the CME pathway by arresting AP2µ function with TyrphostinA23 (**TyrA23**) (Banbury et al., 2003; Dhonukshe et al., 2007) or inhibiting the SDE

pathway by suppressing microdomain formation via sterol solubilization with methyl-β-cyclodextrin (**MβCD**) (Ilangumaran and Hoessli, 1998; Ohtani et al., 1989). MβCD, even at great excess, did not block *flg22*–induced AtRGS1 internalization compared to the control ($p<0.01$) (Figure 2A). Conversely, AtRGS1 internalization induced with glucose was reduced 50% with a minimum concentration of 5mM MβCD (Figure 2B). This suggests that half of the D-glucose-regulated pool of AtRGS1 is located in a SDE domain. To determine if the CME pathway regulates AtRGS1 activity, we applied TyrA23 with *flg22* or D-glucose. AtRGS1 internalization with both activators was significantly reduced ($p<0.01$); completely for flg22-induced AtRGS1 endocytosis (Figure 2C) and by 50% for D-glucose-induced AtRGS1 endocytosis (Figure 2D). The structurally similar but inactive TyrA23 analog TyrphostinA51 showed no significant effect on AtRGS1 internalization ($p<0.01$) (Figure 2C and 2D, TyrA51), indicating that the inhibitory effect of TyrA23 is chemically specific (Banbury et al., 2003). When both inhibitors were applied simultaneously with glucose, AtRGS1 internalization was ablated (Figure 2E). These results suggest that there is a single flg22-induced pool that internalizes through a CME pathway and that there are two distinct glucose-induced pools, one internalizes through the CME pathway and the other through the SDE pathway. Because the glucose-induced pool is equally inhibited by the CME and SDE inhibitors, a rapid equilibrium between the pools is not likely, otherwise neither inhibitor would have shown efficacy.

To further test our hypothesis of ligand-dependent membrane origins of AtRGS1 endocytosis, we used a genetic approach by measuring AtRGS1 internalization in the AP-2μ null mutant, *ap2m* (Kim et al., 2013). The AP-2 complex plays a critical role in transporting cargo in the CME pathway, whereby the μ subunit of this tetrameric AP-2 complex directly interacts with cargo proteins during endocytosis (Bashline et al., 2013; Krauss et al., 2006b). In the *ap2m* mutant

seedlings, flg22-induced AtRGS1 internalization was ablated ($p<0.01$), matching previous results with TyrA23 (Figure 2F). In contrast, glucose resulted in less AtRGS1 internalization in the *ap2m* mutant compared to Col-0 wild type ($p<0.01$). The addition of MβCD with glucose ablated AtRGS1 internalization in the *ap2m* mutant to basal levels (Figure 2G). These observations are consistent with two signal-dependent pools of AtRGS1 on the plasma membrane; a homogenous pool for flg22 signaling and a conglomerate pool for D-glucose signaling.

A Point Mutation in the 7 Transmembrane Domain Disarms Biased Signaling

The μ subunit of the AP-2 complex is a cargo recognition and interaction component in the CME pathway. It binds to known tyrosine motifs, YXXΦ, where X is any amino acid and Φ is an amino acid with a hydrophobic side chain (Ohno et al., 1995). The second cytoplasmic loop in AtRGS1 contains such a motif with the amino acid sequence Y^{112}FIF (Chen et al., 2003). To determine if this motif is necessary for AtRGS1 endocytosis and a potential binding motif for AP-2μ, we generated AtRGS1 with a tyrosine to alanine mutation ($AtRGS1^{Y112A}$). flg22 failed to induce endocytosis of the $AtRGS1^{Y112A}$ mutant (Figure 2H). D-Glucose-induced internalization of the $AtRGS1^{Y112A}$ was reduced to half ($p<0.05$) compared to wild type internalization and was further reduced to the resting level with the addition of MβCD ($p<0.01$) (Figure 2I) demonstrating that the Y^{112}FIF is necessary for internalization and likely a recognition and binding site for AP-2μ. The flg22-induced AtRGS1 pool is entirely mediated by the CME pathway whereas roughly half of the D-glucose-induced AtRGS1 pool internalizes through the CME pathway.

Physically-Distinct, Dynamic Populations of AtRGS1: Architectural Basis for Biased Signaling

We showed through pharmacological and genetics approaches that two signal-dependent pools of AtRGS1 exist raising the possibility that the two AtRGS1 pools are physically distinct on the cell

membrane. The differential dependence on sterol and clathrin for partial glucose- vs. flg22-induced endocytosis of AtRGS1 suggests this is the case. To test this hypothesis, we imaged AtRGS1 with a GFP C-terminal tag using Total Internal Reflection Microscopy (**TIRF**) and IMARIS (v9.2.2, Bitplane Inc) surface tracking (Figure S2 A-E, examples of raw data). We calculated the average size and speed of AtRGS1 proteins during a 30-second interval taken from time-lapse imaging at 5 and at 15 minutes post treatment with glucose and flg22. Two clearly distinct signal-dependent populations of AtRGS1 were observed (Figure 2J). After 5 minutes under glucose conditions, the surface area of AtRGS1-GFP clusters were significantly larger ($\ddot{x}$ = 0.9403 μm^2 n=4619) than flg22 at ($\ddot{x}$ = 0.5998 μm^2 n=2026) (Figure 2J inset) ($p<0.01$). At 15 minutes, the area of flg22 treated AtRGS1-GFP increased slightly to 0.6733 μm^2 (n=1751), with glucose treated AtRGS1-GFP, the area increased to 1.0072 μm^2 (n=6209) (Figure S2 F-H). Velocity differences for AtRGS1-GFP remain consistent between 5 and 15 minutes with flg22-treated AtRGS1 averages at 1.53µm/s and 1.63µm/s, respectively (n= 2026 and 1751) and glucose-treated AtRGS1 averages at 0.98µm/s and 1.01µm/s at 5 and 15 minutes, respectively (n= 4619 and 6209). Two populations of differently sized AtRGS1 protein clusters provides structural support for two origins of endocytosis.

The Signal Dependency Correlates with Endocytosis Marker Redistribution

The Clathrin Light Chain (**CLC**) and Flot1 proteins are associated with CME and SDE, respectively (Fan et al., 2015; Li et al., 2012a). We generated transgenic lines expressing AtRGS1-GFP with either CLC-mCherry or Flot1-mCherry endocytosis markers to investigate the localization of AtRGS1 in relation to both markers. We imaged the response of both endocytosis markers 5 minutes after application of water, flg22, and glucose to look for changes in marker

distribution in the cell (Figure 2K-P). Using Manders Overlap Coefficient, we quantified the co-occurrence of both endocytosis markers with AtRGS1-GFP under all treatment conditions. We are using Manders instead of Pearson's Correlation because our qualitative analysis shows a ligand dependent change in marker localization and shape. We simply want to quantify the change in overlap of the two signals (Manders) and not the change in signal intensity (Pearsons) that may simply be a result of AtRGS1 internalization and not correlated to direct interaction with either endocytosis marker.

A subset of the Manders Overlap Coefficients after background subtraction are shown in Figure 2Q-V and correspond to the confocal micrographs in Figure 2K-P. M1 represents the percentage of total GFP that overlaps with mCherry. Similarly, M2 represents the percentage of total mCherry for CLC or FLOT1 that overlaps with GFP. Under conditions with no signaling ligand (Figure 2K and 2N), RGS1-GFP and our endocytosis markers have a high overlap baseline (Figure 2Q and 2R). Due to the restrictive cytoplasmic space, we believe this is not functional interaction, merely fluorescence overlap due to high protein crowding and resolution limitations. After flg22 addition (Figure 2L and 2O), the proportion of CLC associated with RGS1 decreased, with the proportion of RGS1 overlapping with CLC also decreasing significantly ($p<0.01$) (Figure 2S. Simply stated, a smaller defined subset of the RGS1 and CLC populations are overlapping with each other in a ligand-dependent manner with the endocytosis marker also exhibiting a structural change. This response was not observed with FLOT1 when flg22 was added (Figure 2T). With glucose addition (Figure 2M and 2P) CLC showed no significant change compared to water (Figure 2U), while FLOT1 overlap decreased with RGS1 compared to the water baseline ($p<0.01$) (Figure 2V). The same responses were observed at 15 minutes post ligand addition (Figure S2 I-T). The averages for the entire collection of M2 scores from all samples are presented

in Figure 2W. These results indicate that endocytosis markers are responding to specific ligands and subsets of the total marker and AtRGS1 protein populations are overlapping in a signal specific manner. In summary, the different intrinsic trafficking properties further support at least two pools of ligand-activated AtRGS1.

Signaling Bias Involves Phosphorylation from Different Kinases.

Phosphorylation of AtRGS1 is a necessary requisite for both glucose- and flg22-induced endocytosis. The C-terminus of AtRGS1 contains multiple di-serine residues that could serve as potential phosphorylation sites for signal transduction. A truncated version of AtRGS1 lacking the 43 most C-terminal residues, AtRGS1$^{\Delta Ct}$, served as a blunt phosphorylation-deficient mutation to determine if the C-terminal tail, in particular any C-terminal serines located there are necessary for AtRGS1 endocytosis (Figure S4A). Application of flg22 failed to internalize the AtRGS1$^{\Delta Ct}$ mutant compared to water control ($p<0.01$) (Figure 3A). Glucose application however, internalized the AtRGS1$^{\Delta Ct}$ mutant, but at 50% the level of the wild type AtRGS1 ($p<0.01$). MβCD completely inhibited internalization of the AtRGS1$^{\Delta Ct}$ mutant levels ($p<0.01$) (Figure 3B). These results show that the C-terminus is necessary for flg22- and glucose-induced endocytosis of AtRGS1 and support two subpopulations of AtRGS1 among the glucose-induced pool.

Three phosphorylated serine residues on the C-terminus of AtRGS1 at positions 428, 435, and 436 are necessary for at least partial endocytosis of AtRGS1 induced by both glucose and flg22. Therefore, we mutated these serines to alanine (AtRGS1^{3SA}) to determine if those specific residues were necessary to induce internalization by either agonist. Upon treatment with flg22, AtRGS1^{3SA} internalization was at basal levels compared to wild type ($p<0.01$) (Figure 3C), confirming previous results by Tunc-Ozdemir *et al* (Tunc-Ozdemir et al., 2016) and suggesting that the CME pathway is dependent on phosphorylation of serines 428, 435 and/or 436. In the case

of glucose, endocytosis was only partially impaired by the AtRGS1^{3SA} mutant ($p<0.01$) (Figure 3D). MβCD completely blocked glucose-induced endocytosis of the AtRGS1^{3SA} mutant (Figure 3D), consistent with our previous results that show glucose-induced internalization utilizes both CME and SDE pathways and that the CME pathway requires phosphorylation at $Ser_{428/435/436}$.

These results enable us to exclude an osmotic effect that effectively sequesters a portion of the plasma membrane pool of AtRGS1 into a sterol-dependent, or at least an MβCD-inhibitable, microdomain that is incapable of internalizing its components. If an osmotic effect occurred, the presence of MβCD would have prevented formation of these microdomains and consequently the sequestration of AtRGS1 for the endocytic pool would cause 100% internalization by glucose. This was not observed.

System Bias by Skewed Kinase and G-protein Complex Composition

Because the cluster of phosphorylated serines on the C-terminus of AtRGS1 are required for AtRGS1 internalization, we hypothesize that one mechanism for system bias is to functionally-sequester cognate kinases for glucose and flg22 in their respective ligand-delineated pools. To test this hypothesis, we quantified AtRGS1 internalization in the mutant backgrounds of the flg22-activated FLS2 kinase (*fls2*) and BAK1 co-receptor (*bak1*) and the D-glucose-activated WNK kinase (*wnk8*-2, *wnk1*-1) null mutants. Upon treatment with flg22, AtRGS1 endocytosis was ablated in *fls2* and *bak1-4* mutants ($P<0.01$), while glucose-induced internalization in these mutants was unaffected ($P>0.05$) (Figure 3E and 3F). In contrast, D-glucose-induced internalization in the *wnk8-2* was ablated, while flg22-induced AtRGS1 endocytosis was uneffected ($P=0.89$) (Figure 3G). Interestingly, a low dose, long duration application of 2% glucose over 6 hours to *wnk1-1* had no discernable affect compared to wild type (Figure S3A), prompting a revisit of the proposed mechanism that WNK1 mediates low dose-long duration

activation by glucose (Fu et al., 2014a). Our results suggest that FLS2 and BAK1 are specific to the CME pathway and WNK8 is specific to the SDE pathway.

The canonical components of the heterotrimeric G protein complex are necessary for glucose-induced internalization of AtRGS1 (Fu et al., 2014a; Urano et al., 2012a). More specifically, Gβγ is required for the recruitment of WNK kinases for phosphorylation of AtRGS1, leading to AtRGS1 endocytosis and activation of downstream G signaling. We hypothesized that individual components of the G protein heterotimer may be required for biased signaling. To test this hypothesis, we quantified AtRGS1 endocytosis in G protein mutant backgrounds after flg22 and glucose activation. In the AtGPA1 (Gα) null background, *gpa1-4*, AtRGS1 endocytosis showed no significant difference compared to wild type when glucose was applied ($p<0.01$) (Figure 3H). After addition of flg22, however, AtRGS1 endocytosis was at basal levels ($p < 0.01$ value) in the absence of Gα indicating that the G subunit is essential for this pathway (Figure 3H). We additionally tested AtRGS1 in the absence of XLG2, one member of a three-gene family of atypical, G proteins. XLG proteins have a homologous C-terminal Gα domain and N-terminal nuclear localization signal (Ding et al., 2008). Loss of XLG2 in the *xlg2-1* mutant, did not affect AtRGS1 endocytosis by glucose application ($p= 0.43$), but completely inhibited AtRGS1 endocytosis to basal levels after addition of flg22 ($p<0.01$) (Figure 3I). Additionally, low dose, long duration glucose application had no effect in the *xlg2*-1 mutant compared to wild type (Figure S3B). In the *agb1-2/agg1* double null mutant, AtRGS1 endocytosis was diminished after addition of flg22 ($p<0.01$) (Figure 3J). Loss of the Gβγ dimer in the *agb1-2/agg1* mutant had no effect on glucose-induced AtRGS1 endocytosis compared to wild type after 30 minutes of treatment with 6% D-glucose ($p<0.01$) (Figure 3J). Interestingly, a 2% - 6 hour application of D-glucose required AGB1/AGG1 for activation (Figure 3K).

VPS26 Is a Novel Plant β-arrestin-like Adaptor Necessary for AtRGS1 Endocytosis in the CME Pathway: Discovery and Validation

In the animal G signaling pathway, GPCR endocytosis results in β–arrestin-mediated desensitization of the cell from an extracellular signal. Because plant genomes do not encode canonical arrestins, we sought candidate adaptors for AtRGS1 that may function like β-arrestins to recruit AP2/clathrin to AtRGS1 for endocytosis by querying 3-D structure databases. As shown in Figure S4A and B, we identified three *Arabidopsis* VACUOLAR PROTEIN SORTING 26 (VPS26) proteins that contain arrestin folds (Oliviusson et al., 2006) and are orthologous to human VPS26. *Arabidopsis* VPS26A and VPS26B amino acid sequences are 91% identical whereas VPS26-like is 20% identical to VPS26A and VPS26B. In mammals and plants, VPS26 interacts with VPS29 and VPS35 in the retromer complex on the endosome (Zelazny et al., 2013). This raises the possibility that VPS26 proteins have a moonlighting function in modulating AtRGS1 internalization.

To compare the arrestin and AtVPS26A protein structures, we first created a model of AtVPS26A using MODELLER (Martí-Renom et al., 2000). Toward this, a high quality homogeneous sequence alignment was generated using the VPS26 family (Arabidopsis VPS26A, VPS26B, VPS26like and Homo sapiens VPS26A) and arrestin family (Vertebrates: Human arrestin-1 and arrestin-2; bovine arrestin-1, arrestin-2, arrestin-2, and a variant p44; Squid arrestin-1; and the invertebrate shrimp arrestin (Figure S5A). Human, bovine, and squid sequences were included because PDB structures are available. The squid and shrimp sequences were added for divergence information (among the opistokonts). AtVPS26A and human VPS26A share 56.48% sequence identity while AtVPS26A and arrestin share 14-17% sequence identities (Figure S5B). These results support the use of the high-resolution (2.1Å) crystal structure of *Homo sapiens*

Vps26a (PDB [2FAU]) to generate models of AtVPS26A. Details of the top five selected models are provided in the Methods.

We compared the atvps26a-2 model with the bovine arrestin-3 (PDB [3P2D (Zhan et al., 2011)]). Although the primary amino acid identity between arrestin and AtVPS26A is only ~15% (Figure 4A), the structure of AtVPS26A model shows a remarkably similar arrestin scaffold with arrestin in which contains a semi-symmetric fold of two β strand sandwich structures in the N domain and C domains linked by the central loops with each sandwich formed by 3 or 4 β sheets, respectively.

For arrestin, the conserved structures mainly include the N-terminal and C-terminal arm, central crest comprised of a finger loop (Hirsch et al., 1999), a middle loop (Kim et al., 2012; Shukla et al., 2013); see box ii of Fig. 4) and C loop (Kang et al., 2015) see box I of Fig. 4), Figure 4A), the gate loop, polar core, and the hinge domain (Peterson and Luttrell, 2017). The N-terminal and C-terminal arms stabilize the arrestin conformation. Model atvps26a-2 shares similar N-terminal and C-terminal scaffolds with arrestin however it lacks a short α-helix inside the arrestin N-terminal domain (Figure 4B) which has been implicated in receptor binding (Vishnivetskiy et al., 2011). In addition, arrestin has a longer C-terminal tail, which extend all the way to bind the N terminal domain, important for linkage to enable CME. The C terminus of atvps26a-2 has no extension. Some arrestins also have a short C-tail (Gurevich and Gurevich, 2006).

The overall central crest of atvps26a-2 is similar with that of arrestin which includes the finger loop, middle loop and the C loop (Figure 4C). While arrestin has a longer finger loop important for receptor binding. The rearrangement of the finger loop is a major change associated with arrestin activity, likely serving as a critical part of the activation sensor (Chen et al., 2018).

The polar core is the key component of the phosphate sensor. In arrestin, the polar core is comprised of five charged side chains including two Arg and three Asp that are essential to its activation (Vishnivetskiy et al., 1999). The residues in the polar core of bovine arrestin-3 are: Asp_{27}, Arg_{170}, Asp_{291}, Asp_{298} and Arg_{393} (Figure 4D and E). The human vps26A also contains a polar core between the N terminal and C terminal domains which includes the N domain residues Glu_{119} and Tyr_{121}, and C domain residues Lys_{213}, Glu_{215}, Thr_{258}, Tyr_{272}, and Arg_{296} (Shi et al., 2006). The residues of the polar core of VPS26 are conserved suggesting that they play a critical role in protein function. We thus labeled the polar core of atvps26a according to the human vps26a template. The residues of atvps26a are the N-domain residues Glu_{118} and Tyr_{120}, and C domain residues Arg_{213}, Glu_{215}, Thr_{258}, Tyr_{272}, and Arg_{296} (Figure 4 F and G). Although different amino acid composition, both cores consist of positive charged residues and allow the formation of hydrogen bonds under physiological conditions. However, the orientation and shape of the polar core of VPS26 is distinct from arrestin. The arrestin polar core is embedded between β sheets in the N terminal domain whereas the VPS26 core is open and elongated, spanning the length of space between the N domain and C domain.

The most divergent arrestin structure from 3P2D is a 3Å-resolved truncated arrestin from squid (PDB 1CF1, (Bandyopadhyay et al., 2018). Unlike for bovine arrestin, the C-tail interaction with the gate loop of the polar core is weak and flexible. This functional divergence tempers the impact of the lack of a long C-tail in the atvps26a-2 model.

Taken together, these similarities between AtVPS26 and arrestin prompted the hypothesis that AtVPS26 is a candidate adaptor for CME of AtRGS1. Therefore, we isolated null alleles of the three VPS26 genes in Arabidopsis: VPS26A, VPS26B, and VPS26-LIKE (aka VPS26C) (Jha et al., 2018; Zelazny et al., 2013) and phenotyped the hypocoty length at 5 days, the relevant stage

for our cytological analyses. As shown in Figure S4F, there were no qualitative differences between VPS26 null mutants and Col-0 precluding any developmental basis for alterations in AtRGS1 activation in these mutants. In addition, the AtRGS1-YFP reporter was combined with the mutant backgrounds through generating stable transformants. As shown in Figure 4H, loss of either VPS26A or VPS26B dramatically reduced the flg22-induced internalization of AtRGS1 to levels that are not statistically different from the baseline level ($p=0.34$). Loss of VPS26-like had no statistical effect on AtRGS1 internalization by flg22 ($p=0.65$). Loss of any of the three VPS26 proteins had no statistical effect on glucose-induced internalization of AtRGS1 ($p<0.001$). To confirm that VPS26 is not involved in glucose-induced AtRGS1 internalization, we quantitated the CME and SDE portions of this trafficking pathway in the *vps26* mutants. As shown in Figure 4I, in each of the *vps26* mutant backgrounds, both the TyrA23A and MβCD-inhibitable segments of the glucose-induced internalization of AtRGS1 remained intact. This suggests that the TyrA23-dileneated (CME) pathway used by AtRGS1 when activated by flg22 differs from the TyrA23A-dileneated pathway activated by D-glucose.

The genetic data suggest that VPS26A and B form dimers. To test if VPS26 A and B subunits heterodimerize *in vivo*, BiFC analysis was conducted and showed that heterodimers can form from ectopically-expressed monomers and suggested that the orientation is head-to-tail (Figure 5A). Self-association of arrestin family members also occurs and may be part of a regulatory mechanism for arrestin activation (Chen et al., 2014). For relative quantitation of *in vivo* interaction, split luciferase was performed and found that the strongest interaction was between VPS26A and VPS26B (Figure 5B). VPS26B dimers could form under these conditions but not VPS26A dimers or any oligomer with VPS26Like subunits. We have yet to find conditions which allow stable expression of VPS26 subunits tagged with a full-length auto-fluorescent protein

consistent suggesting that the additional mass of the tag prevents dimer formation and that monomers are unstable.

To test if the full-length AtRGS1 protein interacts with the VPS26 subunits *in vivo*, BiFC, split luciferase, and Y2H analyses were performed. Fluorescent complementation of YFP by AtRGS1-nYFP with cYFP-VPS26A and with VPS26B-cYFP was observed (Figure 5C). The split luciferase assay confirmed that this interaction is as strong as the interaction between AtGPA1 and its AGB1/AGG1 partner (Figure 5D). Finally, Y2H showed that the interaction between AtRGS1 and VPS26 is direct. The entire C-terminal half of AtRGS1 (thus lacking the 7 TM domain) interacts with VPS26B. Surprisingly, removal of the post RGS-box C-terminal tail which includes the $Ser_{428,435,436}$ phosphorylation cluster did not ablate this interaction however, additional loss of two other phosphorylated Ser located between helices VII and VIII of the RGS box completely abolished the interaction.

Biased Signaling Outputs

While both D-glucose and flg22 result in different RGS1-YFP trafficking, we asked what other signaling outputs distinguish these ligands. Two rapid events of the flg22 response is the induction of MITOGEN ACTIVATED PROTEIN KINASE 6 (MPK6) activity and Ca^{2+} signaling (Ranf et al., 2011). To test the impact of flg22 and D-glucose on MPK6 activity in etiolated hypocotyls, we employed a FRET-based sensor that measures kinase activity specifically for MPK6, called *S*ensor *O*f *M*APK *A*ctivity (SOMA) (Zaman et al., 2019). We used SOMA lines tagged with either the human immunodeficiency virus 1 (HIV-1) nuclear export signal (SOMA-NES) or the SV40 nuclear localization signal (SOMA-NLS) (Kalderon et al., 1984; Wen et al., 1995) to measure MPK6 activity in the cytosol or nucleus, respectively. Because these reporters have not been not

validated in hypocotyl epidermal cells, it was necessary to test FRET efficiency in the SOMA lines in response to 150 mM NaCl as a positive control (Droillard et al., 2004). FRET efficiency increased rapidly in SOMA-NES and SOMA-NLS in response to NaCl with no response observed when treated with water (Fig S5 A-D). Additionally, flg22 treatment did not cause substantial FRET efficiency changes in negative control reporter lines: SOMA^{T679A}-NES or SOMA^{T679A}-NLS, which contain mutations in the known phosphorylation site of SOMA that are necessary for FRET changes (Fig S5 E, F). As shown in Figures 5E and F, rapid FRET gains were observed in both SOMA-NES and SOMA-NLS within 2-4 minutes after treatment with flg22. When treated with 6% D-glucose, no change in FRET efficiency was observed, suggesting that D-glucose does not induce activity of MPK6 (Fig 5G and H).

To determine if CME-mediated endocytosis regulates flg22-induced MPK6 activity, we pretreated SOMA-NES lines with TyrA23. TyrA23 successfully blocked the increases in FRET efficiencies that were observed in the absence of the inhibitor (Fig 5 E, replicates in Fig 5 S5 G-N). The negative control TyrA51 showed no significant effect on FRET efficiency after treatment with flg22 (Fig S5 P-V), indicating that the inhibitory effect of TyrA23 is specific to its role in blocking CME-mediated endocytosis and suggesting that AtRGS1 endocytosis, per se, is required. However, we do not exclude the possibility that within the context of flg22-induced MAPK signaling that some other CME-mediated step is rate-limiting.

Because D-glucose utilizes both CME and sterol-dependent pathways to induce AtRGS1 internalization, we tested if the depletion of CME pools of AtRGS1 by D-glucose would alter flg22-induced MPK6 activation. After pretreating SOMA-NES lines with D-glucose for 30 minutes prior to imaging, we found that D-glucose did not have an effect on flg22-increased FRET

efficiency (Fig 5G inset) suggesting that the glucose pool of AtRGS1 is sequestered from the flg22-induced CME of AtRGS1.

We tested the role of D-glucose and flg22 in triggering an increased Ca^{2+} transient response using the intensity-based Ca^{2+} sensor R-GECO1, a red-shifted intensity-based Ca^{2+} reporter (Keinath et al., 2015). We used stable transgenic Arabidopsis lines in wild type and *rgs1-2* backgrounds expressing cytosolic- and nuclear-localized R-GECO1. For our assay, D-glucose and flg22-induced Ca^{2+} signals in wild type and *rgs1-2* plants were measured over a time course in etiolated hypocotyls and normalized against the untreated samples (Fig 5 I, J). Ca^{2+} levels represented by fractional fluorescence changes ($\Delta F/F$; the difference between the fluorescence intensity before and after flg22 application/ initial fluorescence intensity) increased in wild type ($p< 0.01$) while $\Delta F/F$ was greatly diminished (~0.01) in the *rgs1*-2 mutant in response to flg22. D-glucose treatments did not significantly alter the $\Delta F/F$ in Col-0 wild type or *rgs1*-2 mutant, suggesting that D-glucose does not utilize AtRGS1 in a Ca^{2+} branch of the pathway. Despite both D-glucose and flg22 inducing AtRGS1-internalization, these results show that within this context, only flg22 is capable of inducing MPK6 activity and Ca^{2+} changes.

While D-glucose signaling mediated by AtRGS1 does not involve MAPK or Ca^{2+} branches, it does elicit a cellular change; specifically, changes in expression of a small set of genes (Grigston et al., 2008; Urano et al., 2012a). *TRICHOMELESS LIKE 26* (*TBL26*) was shown to be induced by glucose in an AtRGS1/G protein complex-dependent manner (Grigston et al., 2008) and since has been used as a reporter for activation (Fu et al., 2014a; Urano et al., 2016; Urano et al., 2012a). The loss of AtRGS1 inhibits TBL26 expression indicating that genetically, AtRGS1 is a positive modulator of signaling, contradictory to our understanding that RGS proteins negatively modulate G protein activation. One solution to this paradox is that endocytosis of AtRGS1 is

529 required for signal propagation. To test this, we quantitated glucose-induced TBL26 expression in
530 the presence of TyrA23 and found that expression is dramatically reduced. This is consistent with
531 the notion that AtRGS1 signaling has an endosomal origin, analogous to some GPCRs (Eichel and
532 von Zastrow, 2018).

533 **DISCUSSION**

534 The key finding in this study is system bias wherein a single receptor-like RGS protein modulates
535 different quantifiable signaling outputs from two distinct signal inputs (Figure 7A). All of the
536 measured signal outputs correspond to a specific ligand input. For example, flg22 induces ROS,
537 Ca^{2+} release (Figure 6I-K), and MAPK signaling (Figure 6E-H, K)) whereas D-glucose or its
538 metabolite has a measured effect on gene expression (Figure 6L). For flg22, all members of the G
539 protein heterotrimer, along with XLG2 and VPS26A/B are necessary for CME of AtRGS1.
540 Additionally, specific phosphorylation of di-serines at the AtRGS1 C-terminus is required. What
541 is interesting is that glucose signaling that transduces through the same CME of AtRGS1 also
542 requires phosphorylation of the same di-serine residues, but not VPS26 for high dose and low
543 duration sugar exposure (Figure 7B). This phenomenon of signaling through AtRGS1 mediated
544 by the same mechanism of phosphorylation-dependent endocytosis with different G proteins and
545 adapters raises the important question of how are extracellular ligands discriminated for
546 downstream signaling events? Although AtRGS1 endocytosis is necessary for G protein activation
547 it would seem that AtRGS1 is not the discriminator; rather an RLK protein that directly
548 phosphorylates AtRGS1, AtGPA1 and possibly VPS26, to provide the requisite information for
549 ligand-specific downstream signal transduction in the cell.

550 The two mechanisms of AtRGS1 endocytosis induced by D-glucose or its metabolites
551 implies that this signal-dependent pool of AtRGS1 is bipartite, prompting the question of an

552 equilibrium or steady state between the populations. The evidence so far is that it is not. If these
553 AtRGS1 pools were dynamically exchanging within the membrane, we would expect to induce
554 internalization of nearly all membrane bound AtRGS1 by inhibiting one mechanism of endocytosis
555 thereby causing a shift entirely to the other. For example, inhibiting CME with TyrA23 would
556 force AtRGS1 endocytosis entirely to the SDE mode, however this was not observed. Inhibiting
557 one mechanism of endocytosis only partly reduced AtRGS1 internalization, approximately by half,
558 indicating the AtRGS1 populations may be physically isolated and static in the cell membrane
559 (Figure 7C). Some AtRGS1 proteins may be grouped into so-called microdomains or clusters
560 surrounded by receptor/co-receptor RLK proteins while other AtRGS1 may be distributed
561 throughout the membrane without common neighbor RLKs (Figure 7C).

562 Similarly, the question exists whether an equilibrium between the flg22-mediated and D-
563 glucose-mediated CME pools exists and the conclusion is again that equilibria are not likely,
564 consistent with a genuine bias in signaling. To clarify, what we define as the "CME pools" here
565 is the portion of either the flg22- or D-glucose-activated AtRGS1 population that is inhibited by
566 TyrA23, by loss of the tyrosine binding motif, and by loss of the AP2µ subunit of the clathrin
567 complex (Figure 2). While the two pools share these properties, they do not share the requirement
568 of the candidate adapter, VPS26 monomer or dimer (Figure 4). Moreover, when the AtRGS1 pool
569 at the plasma membrane is depleted with D-glucose, there is no effect on the amplitude of flg22
570 activation (Figure 6).

571 The two mechanisms in the composite glucose-induced AtRGS1 endocytosis may be a
572 result of two distinct mechanisms of sugar perception: one through direct interaction of AtRGS1
573 with a sugar or sugar metabolite and the other through sugar binding to a RLK in the membrane
574 similar to flg22::FLS2 binding (Figure 7D). To compare and contrast these two ligand-biased

trajectories, the ordered steps of signal transduction from ligand perception (**step 1**) to internalization of AtRGS1 (**step 5**) are enumerated in Figure 7D to illustrate mechanistically what the present work revealed about each origin of endocytosis including phosphorylation (flg22- **step 2**/glucose- **step 2**), binding of our candidate adaptor VPS26 (flg22- **step 3**), formation of clathrin coated vesicles (flg22- **step 4**/glucose- **step 3**), and finally endocytosis of AtRGS1 either via clathrin coated vesicle (flg22- **step 5** and glucose **step 4**) or sterol dependent rafts (glucose). If glucose or a metabolite is perceived by two distinct sensing mechanisms, each mechanism may operate exclusively through one origin of endocytosis with a unique core of G protein and internalization signaling components. Interestingly, within the glucose model, a system bias may exist favoring one origin of endocytosis that results from architectural differences in the membrane surrounding AtRGS1. A high density of glucose-binding RLKs may favor glucose induced CME of AtRGS1 over the SDE origin.

The division of G protein involvement in glucose-induced CME and SDE challenges previously published reports on the necessity for subunits of the G protein heterotrimer in the full range of glucose signaling through AtRGS1, specifically shown previously, the complete abrogation of AtRGS1 endocytosis in the Gβ null mutant and partial reduction of glucose induced endocytosis with the loss of Gα (Urano et al., 2012a). Our results confirm that Gβ is required for AtRGS1 endocytosis, but only in a low dose scenario, 2% (~110nm). We show no requirement for Gβ or Gα at the higher 6% (~330nm) glucose concentration. It may be that higher sugar concentrations, those typically found at or around vascular unloading areas, illicit a quicker signaling response than low dose sugar likely found in or near epidermal cells where we quantified AtRGS1 internalization. The significance of sugar signaling with regard to cell growth, division, and maintenance may necessitate multiple dose-dependent mechanisms of signal transduction

encoded in different origins of endocytosis and the individual G protein associated components. An investigation of glucose-induced signaling outputs that originate through one or both mechanisms of AtRGS1 endocytosis could reveal information on the significance of each endocytosis origin and if a cell-mediated system bias truly exists.

Both flg22- and D-glucose outputs require AtRGS1 (Chen et al., 2003; Grigston et al., 2008; Liang et al., 2018; Tunc-Ozdemir and Jones, 2017) and an intact heterotrimeric G protein complex (Figure 3) but as discussed for D-glucose responsiveness depends on both the concentration and duration of D-glucose. We previously designated this non-threshold-based activation phenomenon as Dose-Duration Reciprocity (**DDR**) where a low dose of D-glucose for a long period reaches the same output amplitude as a high dose presented as a pulse (Fu et al., 2014a). The proposed mechanism is recruitment of WNK8 and WNK1 to the membrane by the Gβγ dimer AGB1/AGG as a function of DDR to phosphorylate AtRGS1 for endocytosis. However, our higher resolution analyses here challenge some aspects of that mechanism and provide deeper mechanistic insight. AGB1 is not required for high-glucose DDR but is essential for low D-glucose DDR. WNK8 kinase is required as previously shown but WNK1 is shown to not be required at low-glucose longer duration, 6 hours, DDR in contrast to previously published data (Fu, et al 2014). This discrepancy is most likely due to differences in expression level between studies (transient for Fu, et al 2014 and stable here). It has been shown that glucose responsiveness is sensitive to the pool size of AtRGS1 (Liao et al., 2017).

This study focuses on biased signaling launched from different architectures of two AtRGS1-centered pathways. We show that phosphorylation by different sets of kinases encodes this bias. However, the work does not address how the architecture is established or maintained but we speculate that this too is based on a phosphorylation bar code on the AtRGS1/G protein

621 complex. Therefore, establishing the dynamics of both the pre- and post-signaling phosphorylation
622 bar codes is important for our understanding.

623 Why both cytoplasmic and extracellular glucose pools are monitored by the plant cell
624 remains unclear. We speculate that the extracellular pool of glucose is far more dynamic than the
625 cytoplasmic pool due to its rapid metabolic flux in metabolism occurring in the cytoplasm but not
626 occurring in the apoplast. Therefore, an extracellular glucose detection system is more appropriate
627 for monitoring sugars produced by photosynthesis in real time. This is consistent with the recent
628 finding that AtRGS1 is important for detecting fluctuations in CO_2-fixed sugar over the diel cycle
629 (Chen et al., 2003; Tunc-Ozdemir et al., 2018).

630 It is conceivable that the biased system here is the crux of the Defense vs. Growth trade-
631 off problem that plants experience. Specifically, pathogen attack compels the plant to shift its
632 utilization of fixed sugars from building cell walls to defense molecules (Huot et al., 2014). The
633 AtRGS1/G protein complex may be the fulcrum for this balance because it is involved in detecting
634 fixed sugars (Mudgil et al., 2016; Tunc-Ozdemir et al., 2018), establishing cell wall composition
635 (Delgado-Cerezo et al., 2012; Escudero et al., 2017; Klopffleisch et al., 2011) and serving as a
636 sentinel in innate immunity (Zhong et al., 2018).

637 In conclusion, our data provide evidence for system biased signaling through AtRGS1 and
638 introduces a previously unknown arrestin-like adaptor. We introduce the importance of system
639 architecture as it relates to system bias in G protein complex signaling.

640

641

Materials and Methods

Plant Growth Conditions

Arabidopsis seeds were surface sterilized with 80% EtOH for 10 seconds while vortexing followed by a 10-second vortex with 30% bleach. Seeds were subsequently washed 3X with ddH_20 and suspended in 12 well cell culture plates with ¼ MS with no sugar at pH 5.7 with 10-12 seeds per well. Plates were wrapped in aluminum foil and cold-treated at 4˚C for 2 days followed by a 2-hour light treatment to induce germination. After light treatment, plates were again wrapped in aluminum foil and placed on a horizontal shaker at ambient temperature for 5 days before imaging.

AtRGS1 Internalization Assay

AtRGS1-YFP internalization was induced with D-Glucose and flg22 as described in Urano *et al* (Urano et al., 2012b), Fu *et al* (Fu et al., 2014b), and Tunc-Ozdemir *et al* (Tunc-Ozdemir et al., 2016). Briefly, 6% D-glucose or 1µm flg22 were applied to 3-day old seedlings for 30 and 10 minutes respectively before imaging on a Zeiss LSM880 confocal scanning microscope under the conditions described below. Images were acquired on the hypocotyl epidermis 2-4 mm below the cotyledons of seedlings treated with water, glucose, and flg22 in addition to the pharmacological inhibitors outlined below. Seedling exposure to light was minimized as much as is practical while imaging to avoid light induced internalization of AtRGS1.

Pharmacological Inhibition of RGS Internalization

AtRGS1 internalization was inhibited with TyrA23 and MβCD under the following conditions. TyrA23 was applied to 3-day old seedlings for a pre-incubation period of 60 minutes at specified concentrations. Following the pre-incubation period, a combination of TyrA23 and 6% D-Glucose were applied to the seedlings for 30 minutes immediately followed by image acquisition. In the case of flg22, TyrA23 and 1µm flg22 were applied to the seedling for 10 minutes following the

pre-incubation period. For MβCD, the pre-incubation period was 45 minutes at specified concentrations. When both inhibitors were simultaneously applied, pre-incubation was 60 minutes at the respective concentrations.

Confocal Imaging and RGS1 quantification

Image acquisition was done with a Zeiss LSM880 (Zeiss Microscopy, Oberkochen, Germany) confocal laser scanning microscope equipped with AiryScan and GaAsP detection system. YFP excitation was 514nm and emission collection 525-565nm. For RGS internalization assays a z-stack series was acquired with 7-10 focal plane images at 0.5µm intervals with a C-Apochromat 40x/1.2NA water immersion objective. Image processing and RGS internalization measurements were done with the Fiji distribution of ImageJ (Schindelin et al., 2012) as described by Urano *et al (Urano et al., 2012a)* with the following modification: Internalized YFP fluorescence was measured and subtracted from total YFP fluorescence of individual cells as opposed to total fluorescence of the hypocotyl image as stated in Urano *et al*. Statistical analysis was performed using analysis of variance with n=number of cells measured.

TIRF imaging and area/speed measurements of AtRGS1-GFP

Arabidopsis Col-0 seeds containing 35S-RGS1-GFP were grown as mentioned in the plant growth section. 5-day-old seedlings were transferred to a solution of either 6% D-glucose or 1µm flg22 and imaged at 5, 10, and 15 minutes while immersed in the ligand solution. Imaging was performed on a Nikon Ti Eclipse with SR Apo TIRF 100x lens (NA 1.5, WD 120µm). GFP excitation occurred at 488nm and emission collection at 515-555nm with an Andor iXon3 EMCCD camera. 60 second time-lapse imaging was initiated at the beginning of each time point with 200ms acquisition speed. Time-lapse sequences were normalized for fluorescence over time using IMARIS (v9.2.2, Bitplane AG, Zurich, Switzerland). The IMARIS Surface feature was used to

track and calculate the area and speed of individually identifiable AtRGS1 proteins/clusters (labeled as tracks in IMARIS) over time. The average speed and area of each unique Track for a 30 second interval between 5:15-5:45 or 15:15-15:45 was calculated using a script in Matlab (Supplemental code).

Synthesis of [^{14}C] isomaltulose

Sucrose isomerase (SI) from *Pantoea dispersa* UQ68J (GenBank AY223549) was cloned into expression vector pET24b (Novagen) first by PCR of genomic DNA using the following PCR forward primer 5'-GGA TCC AAC AAT GGC AAC GAA TAT ACA AAA GTC C-3'_included a BamH I restriction site and a start codon; reverse primer 5'-ATA GGT ACC TCA GTT CAG CTT ATA GAT CCC-3'_included a Kpn I restriction site and a stop codon.

Expression was done using *E. coli* BL21(DE3) (Novagen), 37°C, 225 rpm. When optical density at 600 nm reached 1.00), isopropyl-D-thiogalactopyranoside was added to a final concentration of 0.5 mM for further induction. The incubation of the culture was continued for another 3 h at 28°C. Cells were harvested by centrifugation (3,000 ×g, 4°C, 10 min), resuspended in 50 mM Tris-HCl (pH 8.0)-2 mM EDTA, and then re-centrifuged. The cell pellet was immediately frozen in liquid nitrogen and stored at -75°C. Cells were suspended in extraction buffer (20 mM Tris-HCl (pH 7.4), 200 mM NaCl, 1 mM EDTA, 1 mM azide, 10 mM -mercaptoethanol) and then lysed by sonication (nine 15-s pulses at 50 W with a Branson Sonifier 450 microprobe), centrifuged (10,000 ×g, 4°C, 10 min), and filtered through a 0.45-µm-pore-size membrane (Gelman Acrodisc). The pET24b vector introduced a carboxy-terminal six-His tag into expressed proteins, which were purified by adsorption to nitrilotriacetic acid (NTA) agarose (QIAGEN) and elution with 25 mM NaH2PO4-150 mM NaCl-125 mM imidazole buffer (pH 8.0)

by following the manufacturer's instructions. The purity of SI proteins was verified by SDS-PAGE as a single band on Coomassie Blue R-250 staining.

[^{14}C] isomaltulose was prepared using 1.48MBq [U-^{14}C]Sucrose (Amersham, UK) in 200 l water with 3% ethanol (equals to 0.3379 mM) was reacted with 30 l purified UQ68J SI for at 30 °C 60 min. The converted [^{14}C] isomatulose concentration by UQ68J sucrose isomerase was estimated by three-rep parallel conversions of unlabelled sucrose (S7903,Sigma) in the same concentration of 0.3379 mM with 3% Ethanol by the same enzyme. BioLC DX600 (Dionex, USA) determinations showed 84.0±0.106% (Mean±SE) was converted into isomaltulose, 3.5±0.197% into trehalulose; into the by-products of glucose and fructose were 4.6±0.072% and 7.8±0.237% respectively; and there was no sucrose left after the reaction was stopped (Figure 1A).

Sugar uptake assay

One-week old seedlings, grown on a filter disc overlaying 1/2X Murashige and Skoog Basal Salts, 0.7% phytogel 23oC, pH 5.8, 8h/d of 100 mole/m2/s1, were lifted off the plate and overlaid 6 mL of water containing approx. 25,000 cpm of [^{14}C] sugars as indicated. The specific activity of the sugars was 12GBq/mmol. At the indicated times, triplicate sets of 10 seedling were gently rinsed and placed in a 1.7-mL microfuge tube with 1 mL of scintillation fluid (Perkin Elmer Inc) and radioactivity was quantitated by liquid scintillation counting. CPM from time zero (typically 80-150 cpm) was subtracted from the average of the 3 samples. The CPM for [^{14}C] isomaltulose uptake into seedlings at each time was corrected for its 84% purity. The experiment as shown was repeated once with the same result. [^{14}C] glucose uptake was repeated 4 times.

G protein activation

Wild type (Col-0) Arabidopsis seeds expressing 35S:AtRGS1-YFP were sterilized and 10-20 seeds were then sown on 1-mL liquid 1/4 X Murashige and Skoog (MS) medium without sucrose

in 24-well plates and stratified at 5oC for 2 days, followed by 2 hours light, then grown in darkness at 27 oC for 4 days. For best results, the plates kept in darkness but moved to the microscope room on the third day to acclimate. A Zeiss LSM710 confocal laser scanning microscope with a C-Apochromat 40X 1.2N.A. water immersion objective was used. The YFP fluorescence was excited by a 514-nm argon laser and the photomultiplier detector was set between 526 nm and 569 nm for quantification. The proportion of internalized AtRGS1 was analyzed by Image J.

Live cell imaging of MAPK reporter (SOMA) lines

Detached etiolated hypocotyls were prepared for imaging on the confocal microscope using the HybriWell™ method as previously described (Vang et al., 2018; Zaman et al., 2019). A hypocotyl from a dark grown 5-day-old seedling was placed on top of the droplet, and a HybriWell™ (Grace Bio-Labs, http://gracebio.com/, cat. no. 611102) was gently placed on the coverslide with the hypocotyl in the center to form a 150-µm deep imaging chamber with a volume of 30 µl. Ultrapure water (300 µl) was injected through one of the HybriWell™ ports using a pipettor to fill the 30-µl chamber with water and to expel any air bubbles. A 200-µl droplet of ultrapure water was then placed on one of the ports to prevent the chamber from drying out. The HybriWells containing the mounted hypocotyls were then placed in covered Petri dishes and equilibrated by incubating at 20–23°C under constant light for 6–8 hours prior to imaging.

Confocal microscopy was performed using a Zeiss LSM 710 with a C-Apochromat 40x/1.20 water immersion objective lens. Samples were excited at 458 nm with 3% power, and emission was measured between 463 and 517 nm for Turquoise GL and between 534 and 570 nm for YPet. Z-stacks were collected every 2 min with an optical slice thickness of 1.2 µm. Chemical treatments were added to the samples during imaging by pipetting 200 µl of solution containing the treatment onto one port of the HybriWell. For experiments involving tyrphostin A23 and

tyrphostin A51, hypocotyls were pretreated with 50 μM of these compounds for 30 min prior to imaging.

Post-processing of the raw image data was performed using Fiji (Schindelin et al., 2012). The 'Z-projection' function was performed on an image stack using the 'Max Intensity' setting. The resulting projection was then separated into two images, one for the Turquoise GL emission channel and one for the YPet emission channel. The 'Subtract Background' function was performed on both images, with the 'rolling-ball radius' set as the default 50 pixels. A mask was then created from the YPet channel using the 'Convert to Mask' function. The background subtracted YPet and Turquoise GL images were then converted into 32-bit images. These 32-bit images were then multiplied by the Mask file. The resulting YPet image was divided by the resulting Turquoise GL image using the 'Image Calculator' function to create a ratio image representing the ratio of YPet to Turquoise emission. Finally, the 'Threshold' function was performed using the default values, with the 'NaN background' option enabled. The 'Fire' lookup table was then applied to the final ratio image. To measure the ratio of YPet to Turquoise GL emission, a region of interest (ROI) was selected within the ratio image using Fiji and the average ratio value within that ROI was then measured.

Live cell Ca^{++} imaging with R-GECO1

5-day-old etiolated hypocotyls expressing R-GECO1 calcium reporter were grown in aqueous media containing ¼ MS. Hypocotyls were excised and mounted in HybriWells 6-8 hours prior to imaging with a Zeiss LSM710 confocal laser scanning microscope equipped with a C-Apochromat 40×/1.20 water immersion objective. R-GECO1 was excited using 561 nm laser with 7.0 % laser power, and emission was measured between 620 and 650 nm. Z-stacks were collected 2 min after chemical treatment with an optical slice thickness of 1.5 μm. Chemical treatments were added to

779 the samples during imaging by pipetting 200 µl of solution containing the treatment onto one port
780 of the HybriWell. The digital images were analyzed with Fiji (Schindelin et al., 2012).

781 *Modeling AtVPS26*

782 Five models (atvps26a1-5) were created by the MODELLER using the automodel script based on
783 the human VPS26A template 2FAU. For evaluation and selection of the "best" model, we
784 calculated the objective function (molpdf), Discrete Optimized Protein Energy (**DOPE**) score,
785 GA341 assessment score and root mean square deviation (**RMSD**) between the model and the
786 template. The best model has the lowest value of the molpdf and overall DOPE assessment scores.
787 In addition, DOPE scores were calculated per-residue and the template and the five atvps26a
788 models were compared using GNUPLOT (Figure S4C) and found to be dissimilar in only three
789 positions (residue around 60, 240, and 260). The atvps26a2 model was selected based on the
790 lowest, RMSD value (Figure S4D) and plotted DOPE per-residue score curve (Fig. S4E). With an
791 RMSD of 0.17 Å, atvps26a-2 differs from the template by less than the length of a C-C bond.

792 **SUPPLEMENTAL INFORMATION**

793 Supplemental Information includes 6 figures and 1 text file.

794 **ACKNOWLEDGEMENTS**

795 We would like to thank Dr. N Phan for creating the AtRGS1^{Y112A} plasmid and transgenic lines and
796 for experiments testing the involvement of adaptors in AtRGS1 endocytosis and data in Figure 1A
797 and B. We thank Dr. V Gurevich for helpful comments and Dr. K Ghusinga for assistance with
798 writing MatLab code. We thank Dr. J Huang for help in the turanose experiment. This work was
799 supported by grants from the NIGMS (GM065989) and NSF (MCB-1713880) to A.M.J. The
800 Division of Chemical Sciences, Geosciences, and Biosciences, Office of Basic Energy Sciences
801 of the US Department of Energy through the grant DE-FG02-05er15671 to A.M.J. funded the

biochemical aspects of this project. The content is solely the responsibility of the authors and does not necessarily represent the official views of the National Institutes of Health.

AUTHOR CONTRIBUTIONS

T.J.R-E., J.W., X.S., B.D., H.J., M.T-O, and F.L. performed experiments and produced figures. T.J.R-E., J.W., X.S., and A.M.J. designed experiments, and analyzed results. P.K provided the MAPK reporters prior to its publication and guided those experiments. L.W. synthesized and purified [^{14}C]isomaltulose. Y.T. performed sugar uptake experiments shown in Figure 1. T.J.R-E., J.W., and A.M.J wrote the paper.

DECLARATION OF INTERESTS

The authors declare no competing interest.

Figure legends

Figure 1. AtRGS1 perceives extracellular glucose or glucose metabolite. flg22 is perceived extracellularly but an extracellular site of glucose perception for activation of G signaling in Arabidopsis has not yet been made with an impermeant glucose analog. See supporting data for this figure in Supplemental Material Figure S1. **A**. Isomaltulose and D-glucose induce rapid AtRGS1-YFP endocytosis in a dose-dependent manner. Images are representative from hypocotyl epidermal cells ectopically expressing AtRGS1 tagged with YFP. **B**. Despite being much less permeant to the Arabidopsis plasma membrane, isomaltulose is slightly more potent than D-glucose in activation of G signaling as measured by proxy using AtRGS1-YFP endocytosis (Fu et al., 2014a). **C**. Turanose is impermeant to plant cells (Rolland et al., 2002) yet is as effective as D-glucose in inducing AtRGS1-YFP endocytosis. **D**. Structures. Both isomaltulose and turanose share a glucose ring moiety.

Figure 2. Two origins of AtRGS1 endocytosis. Pharmacological inhibitors show two origins of AtRGS1-YFP endocytosis. (**A**) AtRGS1-YFP seedlings were treated with increasing concentrations of MβCD at 0mM (n=10), 1mM (n=7), 2mM (n=8), 5mM (8), and 10mM (n=11) for 45 min followed by incubation in the same solution but supplemented with 1 μM flg22 for 10 min or (**B**) 6% D-glucose for 30 min before imaging epidermal cells. Internalized AtRGS1-YFP was quantified to determine total endocytosis of AtRGS1. MβCD does not inhibit flg22-induced AtRGS1 endocytosis, but does partially inhibit glucose-induced AtRGS1 endocytosis at 5mM and above ($p<0.01$). (**C**) TyrphostinA23, an inhibitor of CME, significantly impairs flg22-induced AtRGS1 endocytosis and (**D**) partially inhibits glucose-mediated AtRGS1 endocytosis ($p<0.01$). The structurally similar, but inactive analog of TyrA23, TyrA51, has no effect indicating the effect

of TyrA23 is specific. (**E**) When both inhibitors are applied with glucose, AtRGS1 internalization is reduced to basal levels ($p<0.01$). A genetics approach to inhibit AtRGS1 internalization confirms pharmacological results. (**F**) A genetic null mutant of *ap2μ*, the cargo recognition complex for CME, results in complete inhibition of flg22-induced AtRGS1 down to basal levels, confirming TyrA23 results. (**G**) Glucose-induced internalization of AtRGS1 is partially inhibited in the ap2m mutant, but further reduced to basal levels with the addition of MβCD ($p<0.01$). (**H**) Mutation of Y^{112} to Alanine in the AtRGS1 tyrosine motif recognized by ap2μ, $AtRGS1^{Y112A}$, inhibits flg22-induced AtRGS1 endocytosis to basal levels. (**I**) Glucose-mediated AtRGS1 endocytosis is partially inhibited in $AtRGS1^{Y112A}$, but subsequently reduced to basal levels with the addition of MβCD ($p<0.01$). Quantification of AtRGS1-YFP fluorescence is discussed in methods. (**J**) The speed and surface area of AtRGS1-GFP particles as tracked and measured by IMARIS from 30 second time lapse imaging using TIRF at 5 minutes after treatment with glucose and flg22. Identifiable AtRGS1-GFP particles are significantly smaller in the flg22 treated population compared to glucose. No significant difference in speed is observed between particles in the two treatments. (**K-P**) Endocytosis markers CLC-mCherry and FLOT1-mCherry localize to the cell periphery and increase overlap with RGS1-GFP in a ligand dependent manner after treatment with flg22 and glucose. Zeiss confocal micrographs show AtRGS1-GFP (**green channel**) and either CLC-mCherry (**red channel K-M**) or FLOT1-mCherry (**red channel N-P**) after 5 minute treatments with water (**K and N**), flg22 (**L and O**), and glucose (**M and P**). After water treatment, CLC-mCherry (**K box inset**) and FLOT1-mCherry (**N box inset**) remain distributed throughout the cell cytoplasm and highly overlapped AtRGS1-GFP particles (**Q**). After treatment with flg22, CLC-mCherry migrates to the cell periphery with an observed increase in protein agglomeration (**L red arrows**) and decrease overlap score with RGS1GFP (**S**), while FLOT1-mCherry has no

862 observable change compared to water (**G box inset and R**). Upon treatment with glucose, FLOT1-
863 mCherry protein bodies congregate at the cell periphery (**P red arrows**) and decrease overlap with
864 RGS1-GFP (**V**) , while CLC-mCherry remains unchanged compared to water (**M box inset and**
865 **U**). (**W**) The average overlap scores for CLC-mCherry and FLOT1-mCherry after addition of
866 water, flg22, and glucose. flg22 addition induces a significant change in CLC compared to glucose
867 and water while glucose induces a significant change with FLOT1 compared to flg22 and water
868 $p<0.01$.
869

870 **Figure 3. CME of AtRGS1 is phosphorylation dependent and G protein monomer specific.**
871 Known phosphorylation sites at serine residues on the C-terminal end of AtRGS1 are required for
872 both flg22 and glucose-induced CME of AtRGS1. (**A**) A truncated AtRGS1, AtRGS1$^{\Delta Ct}$, lacking
873 the 43 most C-terminal residues, including 8 serines, resulted in basal levels of flg22-induced
874 AtRGS1 internalization. (**B**) Glucose-induced AtRGS1 internalization is partially reduced in
875 AtRGS1$^{\Delta Ct}$, but further reduced to basal levels with the addition of MβCD. (**C and D**) Mutation
876 of three specific serine residues to alanine at 428, 435, and 436, in a full length AtRGS1,
877 AtRGS1^{3SA}, yielded similar results to AtRGS1$^{\Delta Ct}$ for flg22 and glucose-mediated internalization,
878 but indicate phosphorylation of one or several specific serine residues is necessary for CME of
879 AtRGS1. flg22 and glucose require known kinases for AtRGS1 internalization. (**E**) Genetic
880 ablation of the flg22 receptor FLS2 yields basal levels of flg22-induced AtRGS1 internalization,
881 but does not affect glucose-induced AtRGS1 internalization. (**F**) Similarly, null mutation the
882 BAK1 co-receptor, *bak1-4*, results in ablated flg22-induced AtRGS1 internalization, but not for
883 glucose. (**G**) The high dose and low duration glucose specific WNK8 kinase is necessary for
884 glucose induced AtRGS1 internalization, but not flg22. Individual G proteins are necessary for

AtRGS1 endocytosis in a ligand specific manner. (**H**) A genetic null mutant of Gα, *gpa1-4*, limits flg22-induced endocytosis of AtRGS1 to basal levels, while glucose-induced endocytosis is unaffected compared to wild-type. (**I**) A null mutation of XLG2, *xlg2-1*, an extra-large Gα protein, also results in reduced flg22-induced AtRGS1 endocytosis to basal levels, but has no significant effect on glucose-mediated endocytosis compared to wild type. (**J**) A null mutation of the AGB1/AGG1 heterodimer, *agb1-2/agg1*, inhibited flg22-induced AtRGS1 endocytosis, but had no affect on high does, low duration glucose-induced AtRGS1 endocytosis. (**K**) At low does, long duration AGB1/AGG1 are necessary for glucose induced internalization. Quantification of AtRGS1-YFP fluorescence is discussed in methods.

Figure 4. Arabidopsis VPS26 subunits of the retromer complex may moonlight as β–arrestin-like adaptors for AtRGS1 internalization. (**A)** 3-D alignment of the ATVPS26A model (colored cyan) with the bovine β-arrestin-3 (PDB 3P2D, (colored wheat). The structure of AtVPS26A model shows a similar arrestin scaffold with β arrestin which contains a semi symmetric fold of two β strand sandwich structures in the N domain and C domains linked by the central loops (ii); each sandwich is formed by 3 or 4 β sheets, respectively. (**B)**. Differences between ATVPS24A model and bovine β-arrestin-3. AtVPS26A lacks a short α-helix (i) inside the arrestin N-terminal domain which has been implicated in receptor binding. β arrestin contains a longer C terminal tail which extend all the way to bind the N terminal domain that is important for linkage towards the clathrin-mediated endocytosis (CME) in animals. The C terminus of AtVPS26A has no extension and ends closely to the C domain. (**C**). The central crest. The central crest of atvps26a is similar with that of β arrestin which includes the finger loop, middle loop and

908 the C loop. While β arrestin has a longer finger loop which is important for the receptor binding.
909 D,E The polar c ore of bovine β arrestin-3.The residues in the polar core of bovine β arrestin-3
910 are Asp_{27}, Arg_{170}, Asp_{291}, Asp_{298} and Asp_{393} which are shown as vacuum electrostatics (D) and
911 sticks relatively (**E**). F,G. The polar core of atvps26A. The residues of atvps26a are the N domain
912 residues Glu_{118} and Tyr_{120}, and C domain residues Arg_{213}, Glu_{215}, Thr_{258}, Tyr_{272}, and Arg_{296} which
913 are also shown as vacuum electrostatics (**F**) and sticks (**G**). Although different amino acid
914 composition, both cores consist similarly-positioned positive charged residues and allow the
915 formation of hydrogen bonds under physiological conditions. However, the orientation and shape
916 of the polar core of VPS26 is distinct with β arrestin. The arrestin polar core is embedded between
917 β sheets in the N terminal domain whereas the VPS26 core is open and elongated, spanning the
918 length of space between the N domain and C domain.
919
920 **Figure 5. Physical interaction between AtRGS1 and VPS26.** (**A**) Bifluorescence
921 complementation (BiFC) of VPS26A and VPS26B showing a specific head-to-tail orientation
922 requirement. Representative cells shown. N=5. Experiment repeated 2 times. (**B**) Split luciferase
923 complementation by VPS26A and VPS26B heterodimers and VPS26B homodimers. Error bars
924 are standard error of the mean (SEM). Means with different letters indicate significantly different
925 (Tukey's HSD test, $p<0.05$). N=64 leaf discs from 4 individual tobacco plants. (**C**) BiFC of VPS26
926 A and VPS26B with AtRGS1 in a specific orientation. (**D**) Split luciferase complementation by
927 VPS26A and AtRGS1. Positive control is complementation by the heterotrimeric G protein
928 complex (GPA1/AGB1/AGG1). Negative control is AtGPA1 and AGB1 in the absence of AGG1.
929 Error bars are SEM. N=64. ($p<0.05$). (**E**) Yeast two-hybrid complementation between The
930 cytoplasmic domain of AtRGS1 (RGS1-J5) and VPS26B. RGS1-J5 contains the linker between

the 7TM domain and the RGS box, the RGS box and a C-terminal tail (CT). RGS1- ΔCT lacks the C-terminal tail which contains the phosphorylation cluster required for AtRGS1 endocytosis. RGS1- $\Delta CTS_{405,406A}$ lacks the CT and has two additional phosphosites mutated. –LW is leucine/tryptophan dropout, -LWH is leucine/tryptophan/histidine drop out media; 10 mM 3-AT indicates higher stringency by the addition of 10 mM 3-amino-1,2,4-triazole.

Figure 6. MAPK activation and Ca^{2+} signaling in response to flg22 and D-glucose. (**A-D**) Processed confocal images of the epidermis of etiolated hypocotyls from the SOMA-NLS (**A, B**) and SOMA-NES (**C, D**) transgenic lines depicting the ratio of YPet to Turquoise GL emission produced by exciting Turquoise GL. Scale bar represents 100 µm. Time stamps indicate when the image was collected in minutes:seconds. Images at 00:00 were collected before treatment, while those at time point 20:00 were collected 5 minutes after treatment with 1 µM flg22. White rectangle represent regions of interest (ROIs) used to measure YPet and Turquoise GL emission. (**E-H**). The ratio of YPet to Turquoise GL emission produced by exciting Turquoise GL over time was determined using the ROIs shown in (A-D). During the first 10 minutes of each experiment the samples are incubated in pure water. The arrow indicates the time at which 1 µM flg22 (**E, G**) or 6% D-glucose (**F, H**) was added to the sample. (**E**) SOMA-NES lines pretreated with water (orange) or 50 µM TyrA23 (yellow) prior to imaging. Inset graph (**F**) shows SOMA-NES line pretreated with 6% D-glucose for 30 minutes prior to imaging. (**I**) flg22 dose-response in SOMA-NES lines. flg22 was added after two minutes of imaging. (**J, K**) R-GECO1 lines treated with flg22 or D-glucose in Col-0 (**J**) or *rgs1-2* (**K**) backgrounds. Fluorescence intensity changes of R-GECO1 in ~20 regions of interests in wild type plants. Fractional fluorescence changes (ΔF/F) for R-GECO1 were calculated from background corrected intensity values of R-GECO1 as (F −

954 F0)/F0, where F0 represents the average fluorescence intensity of the baseline of a measurement
955 of each genotype. Error bars are standard deviations. Asterisks represent statistical significance (*P*
956 < 0.01) between treatment and water as determined by 2-way ANOVA.
957
958 **Figure 7. Component overview of flg22 and glucose bias signaling. (A)** Simple model
959 illustrating flg22 and glucose or metabolite input and the respective bias signaling output through
960 AtRGS1, as well as a chart summary detailing the origins of endocytosis (CME and SDE),
961 recognition motif and phosphorylation requirements, and individual proteins necessary for
962 glucose- and flg22-induced endocytosis of AtRGS1. (**B**) Membrane overview illustrating proposed
963 AtRGS1 microdomain clusters with common RLK neighbors. flg22 (orange circle) binds to FLS2
964 to initiate signaling through AtRGS1. The mechanism of glucose (blue circle) perception is
965 unknown as indicated by the question marks. After ligand perception, SDE or CME of AtRGS1
966 occurs to permit downstream signaling. (**C**) A diagram of the individual components involved in
967 the mechanism of endocytosis initiated by flg22 and glucose or metabolite. Numbers indicate the
968 order of operations. For flg22: (1) perception of ligand, (2) phosphorylation of AtRGS1 by a RLK,
969 (3 and 4) binding of clathrin complex and/or VPS26 in an unknown order, and (5) internalization
970 of AtRGS1. For glucose or metabolite: (1) ligand perception by a RLK or direct interaction with
971 AtRGS1, (2) receptor interaction with WNK kinase (In the case of SDE 2 indicates immediate
972 endocytosis as other key components of the pathway are currently unknown), (3) phosphorylation
973 of AtRGS1 by WNK kinases, (4) binding of clathrin complex to AtRGS1, and (5) internalization
974 of AtRGS1. TyrA23 is shown inhibiting CME in both pathways, while MβCD is shown inhibiting
975 AtRGS1 microdomain formation at the membrane.
976

977 **Supplemental Information**

978

979

980 **Supplemental Figure S1**. **Isomaltulose is nearly impermeant in Arabidopsis**. **A**. To test the
981 permeability of Arabidopsis seedlings to isomaltulose, [^{14}C] isomaltulose was synthesized and
982 purified to 84% as described in the STAR* methods. Sugar analysis is as described and the results
983 shown. **B**. Uptake of [^{14}C] D-glucose and [^{14}C] isomaltulose into Arabidopsis seedlings was tested.
984 AU, Arbitrary Units as described.

985

986 **Supplemental Figure S2. Tracking AtRGS1 after ligand addition.** (**A-E**) IMARIS surface
987 tracking showing (**A**) the original wide-field image acquired by TIRF, (**B**) the tracked spots
988 imposed on the original image and tracked at (**C**) 15s, (**D**) 30s, and (**F**) 60s after initiating time-
989 lapse imaging. (**F-H**) Tracking results showing the (**F**) average speed and area for AtRGS1-GFP
990 particles after addition of (**x**) flg22 and (**o**) glucose at 15 minutes post ligand addition. (**G**) area
991 and (**H**) speed of AtRGS1-GFP particles are broken out into proportion of total tracked particles
992 at 15 minutes post ligand addition. (**I-T**) Original field of view confocal micrographs highlighting
993 areas used to calculate Manders Overlap Coefficients from Figure 2K-P (white and yellow boxes)
994 with the addition of 15 minute post ligand addition images.

995

996 **Supplemental Figure S3. G protein involvement in low dose, long duration sugar signaling**
997 (**A**) 2% glucose addition for 6 hours to the genetic null mutant *wnk1-1* shows no discernable
998 difference in AtRGS1 internalization compared to wild type. (**B**) XLG2 is not necessary for
999 AtRGS1 internalization with low-glucose DDR.

Figure S4. Supplemental data used to create the VPS26 model and comparison with arrestin structure described in main figure 4. (**A**) Homogeneous sequence alignment of VPS26 family (Arabidopsis VPS26a, VPS26b, VPS26like and Human VPS26A, VPS26B) with arrestin family (Human arrestin-1, arrestin-2 and bovine arrestin-1, arrestin-2, arrestin-3, squid arrestin-1, shrimp arrestin-1)**.** (**B**) The identity matrix between arrestin family and VPS26 family. Clustal Omega(https://www.ebi.ac.uk/Tools/msa/clustalo/) was used to generate the Multiple Sequence Alignment file and the identity matrix result. Then the ESPript 3.0 (Easy Sequencing in PostScript) which is a program which renders sequence similarities and secondary structure information from aligned sequences for analysis and publication purpose is used to generate the final alignment file(http://espript.ibcp.fr/ESPript/ESPript/index.php). A percentage of equivalent residues is calculated per columns, considering physico-chemical properties. A global score is calculated for all sequences by extracting all possible pairs of residues per columns, for the score greater than similarity GlobalScore (0.7), it will be rendered as coloured characters (red characters on a white background and white characters on a red background if residues are strictly conserved in the column) with blue frames. From the alignment results, AtVPS26a a high sequence identity of 91.06% with AtVPS26b and a 56.48% sequence identity with human VPS26A (shown in red box in figure B). AtVPS26a and arrestin family have around 14-20% sequence identity (shown in red box in the figure). There are conserved residues exist between vps26 family and arrestin family although low sequence identity between them.(1. DpArr1, squid arrestin-1; 2. p44, bovine arrestin-1 splice variant; 3. BtArr3, Bovine Arrestin-3; 4. PmArr1, shrimp arrestin-1; 5. BtArr1, Bovine Arrestin-1; 6. HsArr1, Human Arrestin-1; 7. BtArr2, Bovine Arrestin-2; 8. HsArr2, Human Arrestin-2; 9. AtVPS26like, Arabidopsis VPS26like; 10. AtVPS26A, Arabidopsis VPS26A; 11.

AtVPS26B, Arabidopsis VPS26B; 12. HsVPS26A, human VPS26A; 13. BtVPS26A, bovine VPS26A; 14. HsVPS26B, human VPS26B; 15. BtVPS26B, bovine VPS26B.) (**C**) Model evaluation results of of the 5 models of AtVPS26A. The MODELLER objective function (molpdf), DOPE assessment scores (Discrete Optimized Protein Energy, which is a statistical potential used to assess homology models in protein structure prediction), GA341 assessment score (range from 0.0 (worst) to 1.0 (native-like)) and RMSD (root-mean-square deviation, Å) with the template were calculated to evaluate the models. The "best" model is selected with the lowest value of the molpdf, DOPE score and RMSD value. The second model (atvps26a-2) was selected given better DOPE score and RMSD value. (**D**) DOPE per residue score files of the 5 atvps26a models and the template. DOPE per residue score files of the 5 atvps26a models and the template human VPS26A[2FAU] were plotted using GNUPLOT which is a portable command-line driven graphing utility(http://www.gnuplot.info/).Upper panel is the curves of the 5 atvps26a models and the template. The lower panel is the curve of the "best" model atvps26a-2 with the template. (**E**) 3D structural alignment between AtVPS26A model with human VPS26a template (PDB [2FAU]). Atvps26a-2 model colored in pale-cyan and human VPS26A template colored in bright-orange using pymol. Upper panel: Side view. Lower panel: Top view. (**F**) Etiolated hypocotyls of Col-0 and VPS26 null mutants at 5 days old. Seedlings were germinated and grown in liquid MS for 5 days and transferred to solid agar plates for imaging. Scale bar 5mm.

Supplemental Figure S5. Positive and negative controls for SOMA markers. (**A-D**) (**A**) Transgenic lines SOMA-NLS (Nuclear MAPK reporter) and (**B)** SOMA-NES (cytoplasmic MAPK reporter) were analyzed before and after treatment with 150 mM NaCl as a positive control and with water (**C** and **D**) as the negative control. (**E,F**) Negative control reporters: Mutants of

the transgenic lines SOMA^{T679A}-NLS (**E**) and SOMA^{T679A}-NES (**F)** were treated with 1 µM flg22. (**G - O**) Replicate experimental tracings showing reproducibility of TyrA23 inhibition of the flg22-induced activation of G signaling via AtRGS1-YFP internalization (**G - N**) and its corresponding TyrA51 negative control (**O - V**). During the first 10 minutes of each experiment, SOMA-NES lines pretreated with 50 µM TyrA23 for 10 min (**G - N**) or 50 µM TyrA51 (**O - V**) for 30 minutes prior to activation with flg22. Each graph represents 1 individual hypocotyl and each trace is a region of interest. (**W**) SOMA-NES was pretreated with 6% D-glucose for 30 minutes prior to analysis. Hypocotyls were then treated with 1 µM flg22.

Supplemental Figure S6. Positive and negative controls and dose response. Transgenic lines SOMA-NLS and SOMA-NES were analyzed before and after treatment with 150 mM NaCl as a positive control (**A**, **B**) and water (**C**, **D**). (**E**, **F**) Mutants of the transgenic lines SOMA^{T679A}-NLS and SOMA^{T679A}-NES were treated with 1 µM flg22 during the first 10 minutes of each experiment the samples. SOMA-NES lines were pretreated with 50 µM TyrA23 (**G**-**N**) or 50 µM TyrA51 (**O**-**V**) for 30 minutes prior to imaging. (**W**-**AB**) flg22 dose-response in SOMA-NES lines. (**AC**-**AH**) flg22 dose-response in R-GECO1 lines. Each graph represents 1 individual hypocotyl.

Supplemental Code. MatLab code for averaging unique tracked AtRGS1 particle speed and area. Speed and area data from IMARIS is exported in xls format and imported to MatLab for sorting. Each AtRGS1 tracked protein or cluster has a unique trackID that is sorted while maintaining association with speed and area at defined time points. We identified the start and end location for each unique trackID and created a matrix to store the data and subsequently find the mean for speed and area within our defined time points.

1069

1070

REFERENCES

Adam, T., Bouhidel, K., Der, C., Robert, F., Najid, A., Simon-Plas, F., and Leborgne-Castel, N. (2012). Constitutive expression of clathrin hub hinders elicitor-induced clathrin-mediated endocytosis and defense gene expression in plant cells. FEBS Letters *586*, 3293-3298.

Allen, J.A., Yost, J.M., Setola, V., Chen, X., Sassano, M.F., Chen, M., Peterson, S., Yadav, P.N., Huang, X.-p., Feng, B., *et al.* (2011). Discovery of β-arrestin–biased dopamine D_2 ligands for probing signal transduction pathways essential for antipsychotic efficacy. Proceedings of the National Academy of Sciences *108*, 18488-18493.

Asai, T., Tena, G., Plotnikova, J., Willmann, M.R., Chiu, W.-L., Gomez-Gomez, L., Boller, T., Ausubel, F.M., and Sheen, J. (2002). MAP kinase signalling cascade in Arabidopsis innate immunity. Nature *415*, 977-983.

Banbury, D.N., Oakley, J.D., Sessions, R.B., and Banting, G. (2003). Tyrphostin A23 inhibits internalization of the transferrin Receptor by perturbing the interaction between tyrosine motifs and the medium chain subunit of the AP-2 adaptor complex. J Biol Chem *278*, 12022-12028.

Bandyopadhyay, A., Van Eps, N., Eger, B.T., Rauscher, S., Yedidi, R.S., Moroni, T., West, G.M., Robinson, K.A., Griffin, P.R., Mitchell, J., *et al.* (2018). A novel polar core and weakly fixed C-tail in squid arrestin provide new insight into interaction with rhodopsin. Journal of Molecular Biology *430*, 4102-4118.

Bashline, L., Li, S., Anderson, C.T., Lei, L., and Gu, Y. (2013). The endocytosis of cellulose synthase in Arabidopsis is dependent on μ2, a clathrin-mediated endocytosis adaptin. Plant physiology *163*, 150-160.

Benovic, J., Kuhn, H., Weyand, I., Codina, J., Caron, M., and Lefkowitz, R. (1987). Functional desensitization of the isolated beta-adrenergic receptor by the beta-adrenergic receptor kinase: potential role of an analog of the retinal protein arrestin (48-kDa protein). Proceedings of the National Academy of Sciences of the United States of America *84*, 8879 - 8882.

Benovic, J.L., Strasser, R.H., Caron, M.G., and Lefkowitz, R.J. (1986). Beta-adrenergic receptor kinase: identification of a novel protein kinase that phosphorylates the agonist-occupied form of the receptor. Proceedings of the National Academy of Sciences *83*, 2797-2801.

Bohn, L.M., Gainetdinov, R.R., Lin, F.-T., Lefkowitz, R.J., and Caron, M.G. (2000). μ-Opioid receptor desensitization by β-arrestin-2 determines morphine tolerance but not dependence. Nature *408*, 720-723.

Börnke, F., Hajirezaei, M., Heineke, D., Melzer, M., Herbers, K., and Sonnewald, U. (2002). High-level production of the non-cariogenic sucrose isomer palatinose in transgenic tobacco plants strongly impairs development. Planta *214*, 356-364.

Boucrot, E., Saffarian, S., Zhang, R., and Kirchhausen, T. (2010). Roles of AP-2 in clathrin-mediated endocytosis. PLoS One *5*, e10597.

Butcher, A.J., Prihandoko, R., Kong, K.C., McWilliams, P., Edwards, J.M., Bottrill, A., Mistry, S., and Tobin, A.B. (2011). Differential G-protein-coupled receptor phosphorylation provides evidence for a signaling bar code. Journal of Biological Chemistry *286*, 11506-11518.

Charest, P.G., Oligny-Longpré, G., Bonin, H., Azzi, M., and Bouvier, M. (2007). The V2 vasopressin receptor stimulates ERK1/2 activity independently of heterotrimeric G protein signalling. Cellular Signalling *19*, 32-41.

Chen, J.-G., Willard, F.S., Huang, J., Liang, J., Chasse, S.A., Jones, A.M., and Siderovski, D.P. (2003). A seven-transmembrane RGS protein that modulates plant cell proliferation. Science *301*, 1728-1731.

Chen, L.-Q., Hou, B.-H., Lalonde, S., Takanaga, H., Hartung, M.L., Qu, X.-Q., Guo, W.-J., Kim, J.-G., Underwood, W., Chaudhuri, B., *et al.* (2010). Sugar transporters for intercellular exchange and nutrition of pathogens. Nature *468*, 527.

Chen, Q., Iverson, T.M., and Gurevich, V.V. (2018). Structural basis of arrestin-dependent signal transduction. Trends in Biochemical Sciences *43*, 412-423.

Chen, Q., Zhuo, Y., Kim, M., Hanson, S.M., Francis, D.J., Vishnivetskiy, S.A., Altenbach, C., Klug, C.S., Hubbell, W.L., and Gurevich, V.V. (2014). Self-association of arrestin family members. In Arrestins - Pharmacology and Therapeutic Potential, V.V. Gurevich, ed. (Berlin, Heidelberg, Springer Berlin Heidelberg), pp. 205-223.

Chinchilla, D., Bauer, Z., Regenass, M., Boller, T., and Felix, G. (2006). The *Arabidopsis* receptor kinase FLS2 binds flg22 and determines the specificity of flagellin perception. The Plant Cell *18*, 465-476.

Collins, B.M., McCoy, A.J., Kent, H.M., Evans, P.R., and Owen, D.J. (2002). Molecular architecture and functional model of the endocytic AP2 complex. Cell *109*, 523-535.

DeFea, K.A., Zalevsky, J., Thoma, M.S., Déry, O., Mullins, R.D., and Bunnett, N.W. (2000). β-Arrestin–dependent endocytosis of proteinase-activated receptor 2 is required for intracellular targeting of activated Erk1/2. The Journal of Cell Biology *148*, 1267-1282.

Delgado-Cerezo, M., Sánchez-Rodríguez, C., Escudero, V., Miedes, E., Fernández, P.V., Jordá, L., Hernández-Blanco, C., Sánchez-Vallet, A., Bednarek, P., Schulze-Lefert, P., *et al.* (2012). Arabidopsis heterotrimeric G-protein regulates cell wall defense and resistance to necrotrophic fungi. Molecular Plant *5*, 98-114.

DeWire, S.M., Yamashita, D.S., Rominger, D.H., Liu, G., Cowan, C.L., Graczyk, T.M., Chen, X.-T., Pitis, P.M., Gotchev, D., Yuan, C., *et al.* (2013). A G protein-biased ligand at the μ-opioid

receptor is potently analgesic with reduced gastrointestinal and respiratory dysfunction compared with morphine. Journal of Pharmacology and Experimental Therapeutics *344*, 708-717.

Dhonukshe, P., Aniento, F., Hwang, I., Robinson, D.G., Mravec, J., Stierhof, Y.-D., and Friml, J. (2007). Clathrin-mediated constitutive endocytosis of PIN auxin efflux carriers in Arabidopsis. Current Biology *17*, 520-527.

Ding, L., Pandey, S., and Assmann, S.M. (2008). Arabidopsis extra-large G proteins (XLGs) regulate root morphogenesis. The Plant Journal *53*, 248-263.

Droillard, M.-J., Boudsocq, M., Barbier-Brygoo, H., and Lauriere, C. (2004). Involvement of MPK4 in osmotic stress response pathways in cell suspensions and plantlets of Arabidopsis thaliana: activation by hypoosmolarity and negative role in hyperosmolarity tolerance. FEBS Letters *574*, 42-48.

Eichel, K., and von Zastrow, M. (2018). Subcellular organization of GPCR signaling. Trends in Pharmacological Sciences *39*, 200-208.

Escudero, V., Jordá, L., Sopeña-Torres, S., Mélida, H., Miedes, E., Muñoz-Barrios, A., Swami, S., Alexander, D., McKee, L.S., Sánchez-Vallet, A., *et al.* (2017). Alteration of cell wall xylan acetylation triggers defense responses that counterbalance the immune deficiencies of plants impaired in the β-subunit of the heterotrimeric G-protein. The Plant Journal *92*, 386-399.

Fan, L., Li, R., Pan, J., Ding, Z., and Lin, J. (2015). Endocytosis and its regulation in plants. Trends in Plant Science *20*, 388-397.

Felix, G., Duran, J.D., Volko, S., and Boller, T. (1999). Plants have a sensitive perception system for the most conserved domain of bacterial flagellin. The Plant Journal *18*, 265-276.

Ferguson, K.M., Higashijima, T., Smigel, M.D., and Gilman, A.G. (1986). The influence of bound GDP on the kinetics of guanine nucleotide binding to G proteins. J Biol Chem *261*, 7393-7399.

Fernie, A.R., Roessner, U., and Geigenberger, P. (2001). The sucrose analog palatinose leads to a stimulation of sucrose degradation and starch synthesis when supplied to discs of growing potato tubers. Plant Physiol *125*, 1967-1977.

Fu, Y., Lim, S., Urano, D., Tunc-Ozdemir, M., Phan, N., Elston, T., and Jones, A. (2014a). Reciprocal encoding of signal intensity and duration in a glucose-sensing circuit. . Cell *156*, 1084-1096.

Fu, Y., Lim, S., Urano, D., Tunc-Ozdemir, M., Phan, N.G., Elston, T.C., and Jones, A.M. (2014b). Reciprocal encoding of signal intensity and duration in a glucose-sensing circuit. Cell *156*, 1084-1095.

Géhin, M., Vivat, V., Wurtz, J.-M., Losson, R., Chambon, P., Moras, D., and Gronemeyer, H. (1999). Structural basis for engineering of retinoic acid receptor isotype-selective agonists and antagonists. Chemistry & Biology *6*, 519-529.

Gesty-Palmer, D., Chen, M., Reiter, E., Ahn, S., Nelson, C.D., Wang, S., Eckhardt, A.E., Cowan, C.L., Spurney, R.F., Luttrell, L.M., *et al.* (2006). Distinct β-arrestin- and G protein-dependent pathways for parathyroid hormone receptor-stimulated ERK1/2 activation. Journal of Biological Chemistry *281*, 10856-10864.

Gómez-Gómez, L., and Boller, T. (2000). FLS2: An LRR receptor–like kinase involved in the perception of the bacterial elicitor flagellin in Arabidopsis. Molecular Cell *5*, 1003-1011.

Grigston, J.C., Osuna, D., Scheible, W.R., Stitt, M., and Jones, A.M. (2008). D-glucose sensing by a plasma membrane regulator of G signaling protein, AtRGS1. . FEBS Lett *582*, 3577-3584.
Gurevich, E., and Gurevich, V. (2006). Arrestins: ubiquitous regulators of cellular signaling pathways. Genome Biol *7*, 236.

Hao, H., Fan, L., Chen, T., Li, R., Li, X., He, Q., Botella, M.A., and Lin, J. (2014). Clathrin and membrane microdomains cooperatively regulate RbohD dynamics and activity in *Arabidopsis*. The Plant Cell *26*, 1729-1745.

Hirsch, J., Schubert, C., Gurevich, V., and Sigler, P. (1999). The 2.8 A crystal structure of visual arrestin: a model for arrestin's regulation. Cell *97*, 257 - 269.

Huot, B., Yao, J., Montgomery, B.L., and He, S.Y. (2014). Growth–defense tradeoffs in plants: A balancing act to optimize fitness. Molecular Plant *7*, 1267-1287.

Ilangumaran, S., and Hoessli, D.C. (1998). Effects of cholesterol depletion by cyclodextrin on the sphingolipid microdomains of the plasma membrane. Biochemical Journal *335*, 433-440.

Irani, N.G., Di Rubbo, S., Mylle, E., Van den Begin, J., Schneider-Pizoń, J., Hniliková, J., Šíša, M., Buyst, D., Vilarrasa-Blasi, J., Szatmári, A.-M., *et al.* (2012). Fluorescent castasterone reveals BRI1 signaling from the plasma membrane. Nature chemical biology *8*, 583.

Jackson, L.P., Kelly, B.T., McCoy, A.J., Gaffry, T., James, L.C., Collins, B.M., Höning, S., Evans, P.R., and Owen, D.J. (2010). A large-scale conformational change couples membrane recruitment to cargo binding in the AP2 clathrin adaptor Complex. Cell *141*, 1220-1229.

Jelenska, J., Davern, S.M., Standaert, R.F., Mirzadeh, S., and Greenberg, J.T. (2017). Flagellin peptide flg22 gains access to long-distance trafficking in Arabidopsis via its receptor, FLS2. Journal of Experimental Botany *68*, 1769-1783.

Jha, S.G., Larson, E.R., Humble, J., Domozych, D.S., Barrington, D.S., and Tierney, M.L. (2018). Vacuolar Protein Sorting 26C encodes an evolutionarily conserved large retromer subunit in

eukaryotes that is important for root hair growth in Arabidopsis thaliana. The Plant Journal *94*, 595-611.

Johnston, C.A., Taylor, J.P., Gao, Y., Kimple, A.J., Grigston, J.C., Chen, J.-G., Siderovski, D.P., Jones, A.M., and Willard, F.S. (2007). GTPase acceleration as the rate-limiting step in Arabidopsis G protein-coupled sugar signaling. Proceedings of the National Academy of Sciences *104*, 17317-17322.

Jones, J., Duffy, J., M, M., Temple, B., Dohlman, H., and Jones, A. (2011a). The crystal structure of a self-activating G protein α subunit reveals its distinct mechanism of signal initiation. Sci Signal *4*, ra8.

Jones, J.C., Temple, B.R.S., Jones, A.M., and Dohlman, H.G. (2011b). Functional reconstitution of an atypical G protein heterotrimer and regulator of G protein signaling protein (RGS1) from *Arabidopsis thaliana*. Journal of Biological Chemistry *286*, 13143-13150.

Kalderon, D., Roberts, B.L., Richardson, W.D., and Smith, A.E. (1984). A short amino acid sequence able to specify nuclear location. Cell *39*, 499-509.

Kang, Y., Zhou, X.E., Gao, X., He, Y., Liu, W., Ishchenko, A., Barty, A., White, T.A., Yefanov, O., Han, G.W., *et al.* (2015). Crystal structure of rhodopsin bound to arrestin by femtosecond X-ray laser. Nature *523*, 561.

Keinath, N.F., Waadt, R., Brugman, R., Schroeder, Julian I., Grossmann, G., Schumacher, K., and Krebs, M. (2015). Live cell imaging with R-GECO1 sheds light on flg22- and chitin-induced transient $[Ca^{2+}]_{cyt}$ patterns in Arabidopsis. Molecular Plant *8*, 1188-1200.

Kelly, B.T., McCoy, A.J., Späte, K., Miller, S.E., Evans, P.R., Höning, S., and Owen, D.J. (2008). A structural explanation for the binding of endocytic dileucine motifs by the AP2 complex. Nature *456*, 976.

Kim, M., Vishnivetskiy, S.A., Van Eps, N., Alexander, N.S., Cleghorn, W.M., Zhan, X., Hanson, S.M., Morizumi, T., Ernst, O.P., Meiler, J., *et al.* (2012). Conformation of receptor-bound visual arrestin. Proceedings of the National Academy of Sciences *109*, 18407-18412.

Kim, S.Y., Xu, Z.-Y., Song, K., Kim, D.H., Kang, H., Reichardt, I., Sohn, E.J., Friml, J., Juergens, G., and Hwang, I. (2013). Adaptor protein complex 2–mediated endocytosis is crucial for male reproductive organ development in *Arabidopsis*. The Plant Cell *25*, 2970-2985.

Klopffleisch, K., Phan, N., Augustin, K., Bayne, R.S., Booker, K.S., Botella, J.R., Carpita, N.C., Carr, T., Chen, J.-G., Cooke, T.R., *et al.* (2011). Arabidopsis G-protein interactome reveals connections to cell wall carbohydrates and morphogenesis. Mol Syst Biol *7*, 532.

Krauss, M., Kukhtina, V., Pechstein, A., and Haucke, V. (2006a). Stimulation of phosphatidylinositol kinase type I-mediated phosphatidylinositol (4,5)-bisphosphate synthesis by AP-2μ–cargo complexes. Proceedings of the National Academy of Sciences *103*, 11934-11939.

Krauss, M., Kukhtina, V., Pechstein, A., and Haucke, V. (2006b). Stimulation of phosphatidylinositol kinase type I-mediated phosphatidylinositol (4, 5)-bisphosphate synthesis by AP-2μ–cargo complexes. Proceedings of the National Academy of Sciences *103*, 11934-11939.

Lee, J., Eschen-Lippold, L., Lassowskat, I., Böttcher, C., and Scheel, D. (2015). Cellular reprogramming through mitogen-activated protein kinases. Frontiers in Plant Science *6*.

Li, L., and Sheen, J. (2016). Dynamic and diverse sugar signaling. Current Opinion in Plant Biology *33*, 116-125.

Li, R., Liu, P., Wan, Y., Chen, T., Wang, Q., Mettbach, U., Baluška, F., Šamaj, J., Fang, X., Lucas, W.J., *et al.* (2012a). A Membrane Microdomain-Associated Protein, Arabidopsis Flot1, Is Involved in a Clathrin-Independent Endocytic Pathway and Is Required for Seedling Development. The Plant Cell *24*, 2105-2122.

Li, R., Liu, P., Wan, Y., Chen, T., Wang, Q., Mettbach, U., Baluška, F., Šamaj, J., Fang, X., Lucas, W.J., *et al.* (2012b). A membrane microdomain-associated protein, Arabidopsis Flot1, is involved in a clathrin-independent endocytic pathway and is required for seedling development. The Plant Cell *24*, 2105-2122.

Li, X., Wang, X., Yang, Y., Li, R., He, Q., Fang, X., Luu, D.-T., Maurel, C., and Lin, J. (2011). Single-molecule analysis of PIP2;1 Dynamics and partitioning reveals multiple modes of *Arabidopsis* plasma membrane aquaporin regulation. The Plant Cell *23*, 3780-3797.

Liang, X., Ma, M., Zhou, Z., Wang, J., Yang, X., Rao, S., Bi, G., Li, L., Zhang, X., Chai, J., *et al.* (2018). Ligand-triggered de-repression of Arabidopsis heterotrimeric G proteins coupled to immune receptor kinases. Cell Research.

Liao, K.-L., Melvin, C.E., Sozzani, R., Jones, R.D., Elston, T.C., and Jones, A.M. (2017). Dose-Duration Reciprocity for G protein activation: Modulation of kinase to substrate ratio alters cell signaling. PLoS ONE *12*, e0190000.

Lin, W.-W., and Hsieh, S.-L. (2011). Decoy receptor 3: A pleiotropic immunomodulator and biomarker for inflammatory diseases, autoimmune diseases and cancer. Biochemical Pharmacology *81*, 838-847.

Lohse, M., Benovic, J., Codina, J., Caron, M., and Lefkowitz, R. (1990). beta-Arrestin: a protein that regulates beta-adrenergic receptor function. Science *248*, 1547 - 1550.

Loreti, E., Alpi, A., and Perata, P. (2000). Glucose and disaccharide-sensing mechanisms modulate the expression of alpha -amylase in barley embryos. Plant Physiol *123*, 939-948.

Luttrell, L.M., Roudabush, F.L., Choy, E.W., Miller, W.E., Field, M.E., Pierce, K.L., and Lefkowitz, R.J. (2001). Activation and targeting of extracellular signal-regulated kinases by β-arrestin scaffolds. Proceedings of the National Academy of Sciences *98*, 2449-2454.

Manglik, A., Lin, H., Aryal, D.K., McCorvy, J.D., Dengler, D., Corder, G., Levit, A., Kling, R.C., Bernat, V., Hübner, H., *et al.* (2016). Structure-based discovery of opioid analgesics with reduced side effects. Nature *537*, 185.

Martí-Renom, M.A., Stuart, A.C., Fiser, A., Sánchez, R., and, F.M., and Šali, A. (2000). Comparative protein structure modeling of genes and genomes. Annual Review of Biophysics and Biomolecular Structure *29*, 291-325.

Mudgil, Y., Karve, A., Teixeira, P., Jiang, K., Tunc-Ozdemir, M., and Jones, A. (2016). Photosynthate regulation of the root system architecture mediated by the heterotrimeric G protein complex in Arabidopsis. Frontiers in Plant Science *7*.

Nobles, K.N., Xiao, K., Ahn, S., Shukla, A.K., Lam, C.M., Rajagopal, S., Strachan, R.T., Huang, T.-Y., Bressler, E.A., Hara, M.R., *et al.* (2011). Distinct phosphorylation sites on the β_2-adrenergic receptor establish a barcode that encodes differential functions of β-arrestin. Science Signaling *4*, ra51-ra51.

Ohno, H., Stewart, J., Fournier, M., Bosshart, H., Rhee, I., Miyatake, S., Saito, T., Gallusser, A., Kirchhausen, T., and Bonifacino, J. (1995). Interaction of tyrosine-based sorting signals with clathrin-associated proteins. Science *269*, 1872-1875.

Ohtani, Y., Irie, T., Uekama, K., Fukunaga, K., and Pitha, J. (1989). Differential effects of alpha-, beta- and gamma-cyclodextrins on human erythrocytes. Eur J Biochem *186*, 17-22.

Oliviusson, P., Heinzerling, O., Hillmer, S., Hinz, G., Tse, Y.C., Jiang, L., and Robinson, D.G. (2006). Plant retromer, Localized to the prevacuolar compartment and microvesicles in *Arabidopsis*, may interact with vacuolar sorting receptors. The Plant Cell *18*, 1239-1252.

Pan, G., Ni, J., Wei, Y.-F., Yu, G.-l., Gentz, R., and Dixit, V.M. (1997). An antagonist decoy receptor and a death domain-containing receptor for TRAIL. Science *277*, 815-818.

Peterson, Y.K., and Luttrell, L.M. (2017). The diverse roles of arrestin scaffolds in G protein–coupled receptor signaling. Pharmacological Reviews *69*, 256-297.

Pharr, D., and Keller, F. (2017). In photoassimilate distribution plants and crops source-sink relationships (Routledge), pp. 157-183.

Raffaele, S., Bayer, E., Lafarge, D., Cluzet, S., German Retana, S., Boubekeur, T., Leborgne-Castel, N., Carde, J.-P., Lherminier, J., Noirot, E., *et al.* (2009). Remorin, a solanaceae protein resident in membrane rafts and plasmodesmata, impairs potato virus X movement. The Plant Cell *21*, 1541-1555.

Rajagopal, S., Kim, J., Ahn, S., Craig, S., Lam, C.M., Gerard, N.P., Gerard, C., and Lefkowitz, R.J. (2010a). β-arrestin- but not G protein-mediated signaling by the "decoy" receptor CXCR7. Proceedings of the National Academy of Sciences *107*, 628-632.

Rajagopal, S., Rajagopal, K., and Lefkowitz, R.J. (2010b). Teaching old receptors new tricks: biasing seven-transmembrane receptors. Nature Reviews Drug Discovery *9*, 373.

Ranf, S., Eschen-Lippold, L., Pecher, P., Lee, J., and Scheel, D. (2011). Interplay between calcium signalling and early signalling elements during defence responses to microbe- or damage-associated molecular patterns. The Plant Journal *68*, 100-113.

Rives, M.-L., Rossillo, M., Liu-Chen, L.-Y., and Javitch, J.A. (2012). 6′-Guanidinonaltrindole (6′-GNTI) is a G protein-biased κ-opioid receptor agonist that inhibits arrestin recruitment. Journal of Biological Chemistry *287*, 27050-27054.

Rolland, F., Moore, B., and Sheen, J. (2002). Sugar sensing and signaling in plants. The Plant Cell *14*, S185-S205.

Schindelin, J., Arganda-Carreras, I., Frise, E., Kaynig, V., Longair, M., Pietzsch, T., Preibisch, S., Rueden, C., Saalfeld, S., Schmid, B., *et al.* (2012). Fiji: an open-source platform for biological-image analysis. Nature Methods *9*, 676.

Shenoy, S.K., Drake, M.T., Nelson, C.D., Houtz, D.A., Xiao, K., Madabushi, S., Reiter, E., Premont, R.T., Lichtarge, O., and Lefkowitz, R.J. (2006). β-Arrestin-dependent, G protein-independent ERK1/2 activation by the β2 adrenergic receptor. Journal of Biological Chemistry *281*, 1261-1273.

Shi, H., Rojas, R., Bonifacino, J.S., and Hurley, J.H. (2006). The retromer subunit Vps26 has an arrestin fold and binds Vps35 through its C-terminal domain. Nature Structural & Molecular Biology *13*, 540-548.

Shiraishi, Y., Natsume, M., Kofuku, Y., Imai, S., Nakata, K., Mizukoshi, T., Ueda, T., Iwaï, H., and Shimada, I. (2018). Phosphorylation-induced conformation of β2-adrenoceptor related to arrestin recruitment revealed by NMR. Nature Communications *9*, 194.

Shiu, S.H., and Bleecker, A.B. (2001). Plant receptor-llike gene family: diversity, function, and signaling. Science STKE *Dec. 18th*, RE22.

Shukla, A.K., Manglik, A., Kruse, A.C., Xiao, K., Reis, R.I., Tseng, W.-C., Staus, D.P., Hilger, D., Uysal, S., Huang, L.-Y., *et al.* (2013). Structure of active β-arrestin-1 bound to a G-protein-coupled receptor phosphopeptide. Nature *497*, 137.

Sibley, D.R., Benovic, J.L., Caron, M.G., and Lefkowitz, R.J. (1987). Regulation of transmembrane signaling by receptor phosphorylation. Cell *48*, 913-922.

Sinha, A.K., Hofmann, M.G., Romer, U., Kockenberger, W., Elling, L., and Roitsch, T. (2002). Metabolizable and non-metabolizable sugars activate different signal transduction pathways in tomato. Plant Physiol *128*, 1480-1489.

Smith, J.S., Lefkowitz, R.J., and Rajagopal, S. (2018). Biased signalling: from simple switches to allosteric microprocessors. Nature Reviews Drug Discovery *17*, 243.

Sun, Y., Li, L., Macho, A.P., Han, Z., Hu, Z., Zipfel, C., Zhou, J.-M., and Chai, J. (2013). Structural basis for flg22-induced activation of the *Arabidopsis* FLS2-BAK1 immune complex. Science *342*, 624-628.

Tunc-Ozdemir, M., and Jones, A.M. (2017). Ligand-induced dynamics of heterotrimeric G protein-coupled receptor-like kinase complexes. PLoS ONE *12*, e0171854.

Tunc-Ozdemir, M., Li, B., Jaiswal, D.K., Urano, D., Jones, A.M., and Torres, M.P. (2017). Predicted functional implications of phosphorylation of regulator of G protein signaling protein in plants. Frontiers in Plant Science *8*.

Tunc-Ozdemir, M., Liao, K.-L., Ross-Elliott, T.J., Elston, T.C., and Jones, A.M. (2018). Long-distance communication in Arabidopsis involving a self-activating G protein. Plant Direct *2*, e00037.

Tunc-Ozdemir, M., Urano, D., Jaiswal, D.K., Clouse, S.D., and Jones, A.M. (2016). Direct modulation of heterotrimeric G protein-coupled signaling by a receptor kinase complex. Journal of Biological Chemistry *291*, 13918-13925.

Urano, D., Maruta, N., Trusov, Y., Stoian, R., Liang, Y., Jaiswal, D., Thung, L., Botella, J., and Jones, A. (2016). Saltatory evolution of the heterotrimeric G protein signaling mechanisms in the plant kingdom. Science Signaling *9*, ra93.

Urano, D., Phan, N., Jones, J.C., Yang, J., Huang, J., Grigston, J., Philip Taylor, J., and Jones, A.M. (2012a). Endocytosis of the seven-transmembrane RGS1 protein activates G-protein-coupled signalling in Arabidopsis. Nat Cell Biol *14*, 1079-1088.

Urano, D., Phan, N., Jones, J.C., Yang, J., Huang, J., Grigston, J., Taylor, J.P., and Jones, A.M. (2012b). Endocytosis of the seven-transmembrane RGS1 protein activates G-protein-coupled signalling in Arabidopsis. Nature Cell Biology *14*, 1079-1088.

Urs, N.M., Gee, S.M., Pack, T.F., McCorvy, J.D., Evron, T., Snyder, J.C., Yang, X., Rodriguiz, R.M., Borrelli, E., Wetsel, W.C., *et al.* (2016). Distinct cortical and striatal actions of a β-arrestin–biased dopamine D2 receptor ligand reveal unique antipsychotic-like properties. Proceedings of the National Academy of Sciences *113*, E8178-E8186.

Urs, N.M., Peterson, S.M., and Caron, M.G. (2017). New concepts in dopamine D2 receptor biased signaling and implications for schizophrenia therapy. Biological Psychiatry *81*, 78-85.

Vang, S., Seitz, K., and Krysan, P. (2018). A simple microfluidic device for live cell imaging of Arabidopsis cotyledons, leaves, and seedlings. Biotechniques *64*, 255-261.

Vishnivetskiy, S.A., Gimenez, L.E., Francis, D.J., Hanson, S.M., Hubbell, W.L., Klug, C.S., and Gurevich, V.V. (2011). Few residues within an extensive binding interface drive receptor interaction and determine the specificity of arrestin proteins. Journal of Biological Chemistry *286*, 24288-24299.

Vishnivetskiy, S.A., Paz, C.L., Schubert, C., Hirsch, J.A., Sigler, P.B., and Gurevich, V.V. (1999). How does arrestin respond to the phosphorylated state of rhodopsin? Journal of Biological Chemistry *274*, 11451-11454.

Wen, W., Meinkotht, J.L., Tsien, R.Y., and Taylor, S.S. (1995). Identification of a signal for rapid export of proteins from the nucleus. Cell *82*, 463-473.

White, K.L., Robinson, J.E., Zhu, H., DiBerto, J.F., Polepally, P.R., Zjawiony, J.K., Nichols, D.E., Malanga, C.J., and Roth, B.L. (2015). The G protein–biased opioid receptor agonist RB-64 is analgesic with a unique spectrum of activities *in vivo*. Journal of Pharmacology and Experimental Therapeutics *352*, 98-109.

Williams, L.E., Lemoine, R., and Sauer, N. (2000). Sugar transporters in higher plants – a diversity of roles and complex regulation. Trends in Plant Science *5*, 283-290.

Wingler, L.M., Elgeti, M., Hilger, D., Latorraca, N.R., Lerch, M.T., Staus, D.P., Dror, R.O., Kobilka, B.K., Hubbell, W.L., and Lefkowitz, R.J. (2019). Angiotensin analogs with divergent bias stabilize distinct receptor conformations. Cell *176*, 468-478.e411.

Wu, L., and Birch, R. (2011). Isomaltulose is actively metabolized in plant cells. Plant Physiol *157*, 2094-2101.

Yang, F., Yu, X., Liu, C., Qu, C.-X., Gong, Z., Liu, H.-D., Li, F.-H., Wang, H.-M., He, D.-F., Yi, F., *et al.* (2015). Phospho-selective mechanisms of arrestin conformations and functions revealed by unnatural amino acid incorporation and 19F-NMR. Nature Communications *6*, 8202.

Yang, Z., Yang, F., Zhang, D., Liu, Z., Lin, A., Liu, C., Xiao, P., Yu, X., and Sun, J.-P. (2017). Phosphorylation of G Protein-Coupled Receptors: From the Barcode Hypothesis to the Flute Model. Molecular pharmacology *92*, 201-210.

Zaman, N., Seitz, K., Kabir, M., George-Schreder, L.S., Shepstone, I., Liu, Y., Zhang, S., and Krysan, P.J. (2019). A Förster resonance energy transfer sensor for live-cell imaging of mitogen-activated protein kinase activity in Arabidopsis. The Plant Journal *97*, 970-983.

Zelazny, E., Santambrogio, M., Pourcher, M., Chambrier, P., Berne-Dedieu, A., Fobis-Loisy, I., Miège, C., Jaillais, Y., and Gaude, T. (2013). Mechanisms governing the endosomal membrane recruitment of the core retromer in Arabidopsis. Journal of Biological Chemistry *288*, 8815-8825.

Zhan, X., Gimenez, L.E., Gurevich, V.V., and Spiller, B.W. (2011). Crystal structure of arrestin-3 reveals the basis of the difference in receptor binding between two non-visual subtypes. Journal of Molecular Biology *406*, 467-478.

Zhong, C.-L., Zhang, C., and Liu, J.-Z. (2018). Heterotrimeric G protein signaling in plant immunity. Journal of Experimental Botany *70*, 1109-1118.

Figure 1

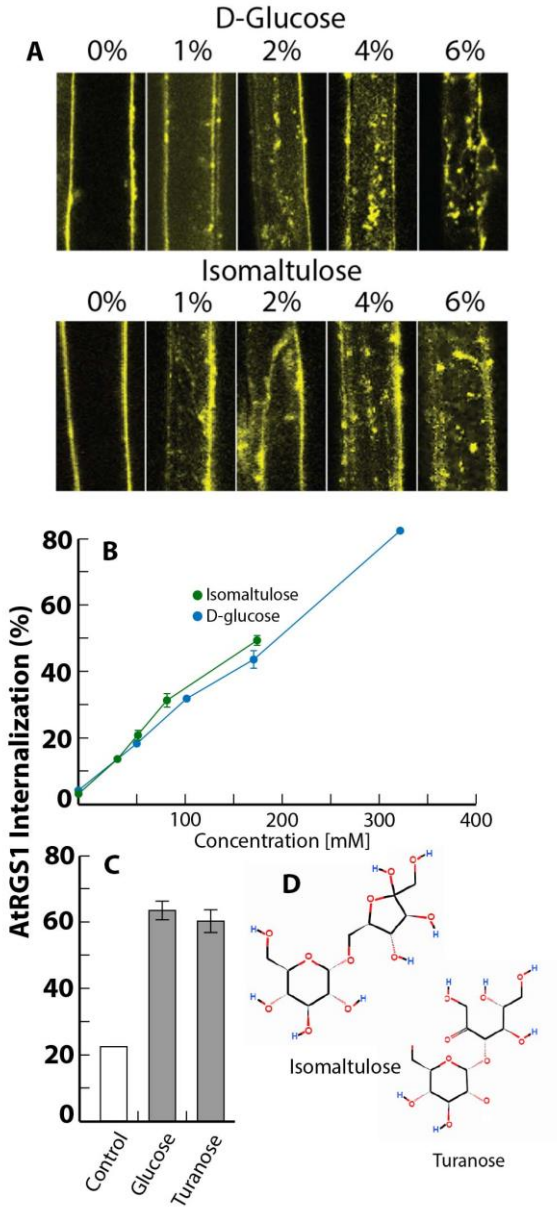

Figure 2

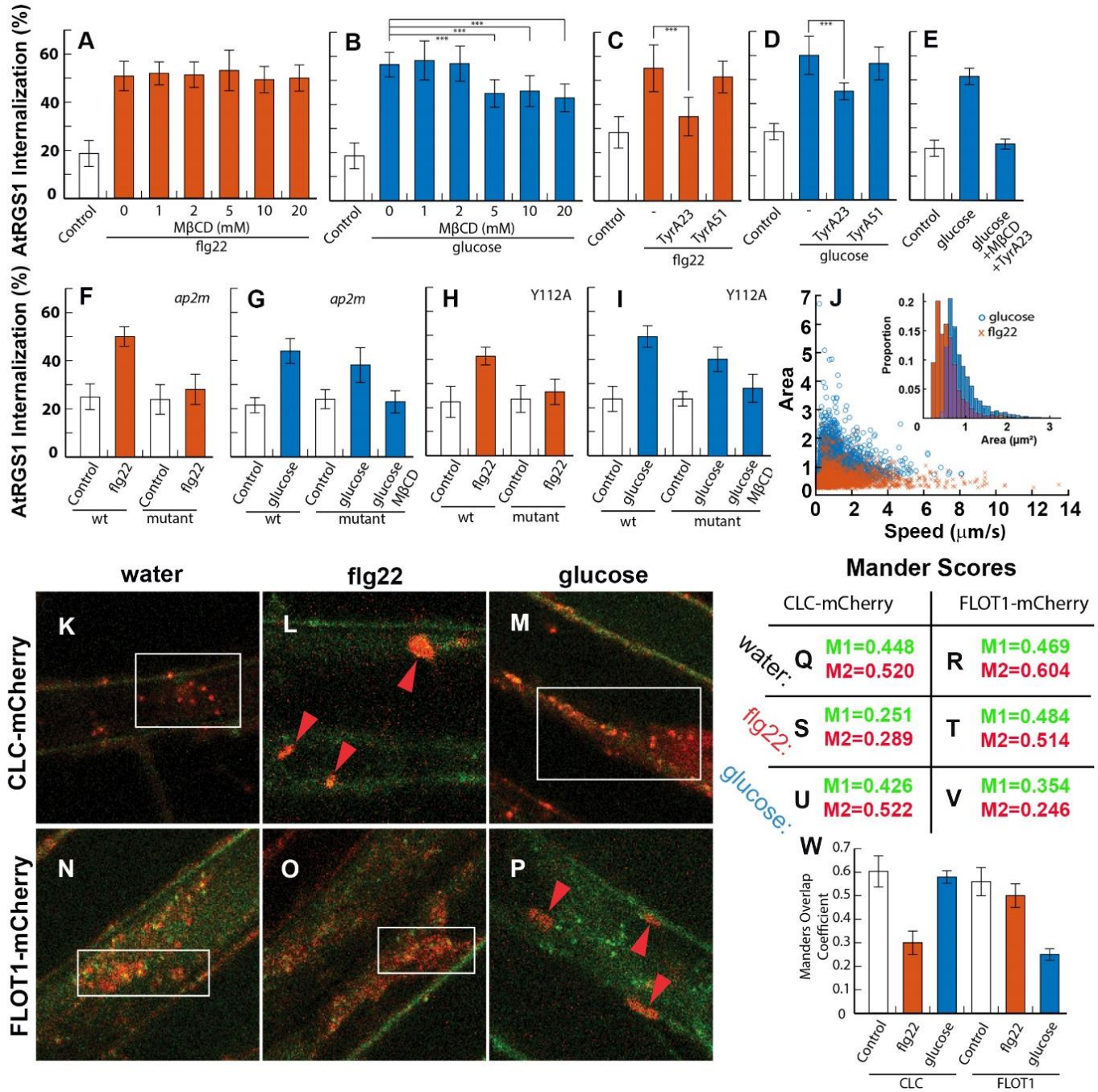

Figure 3

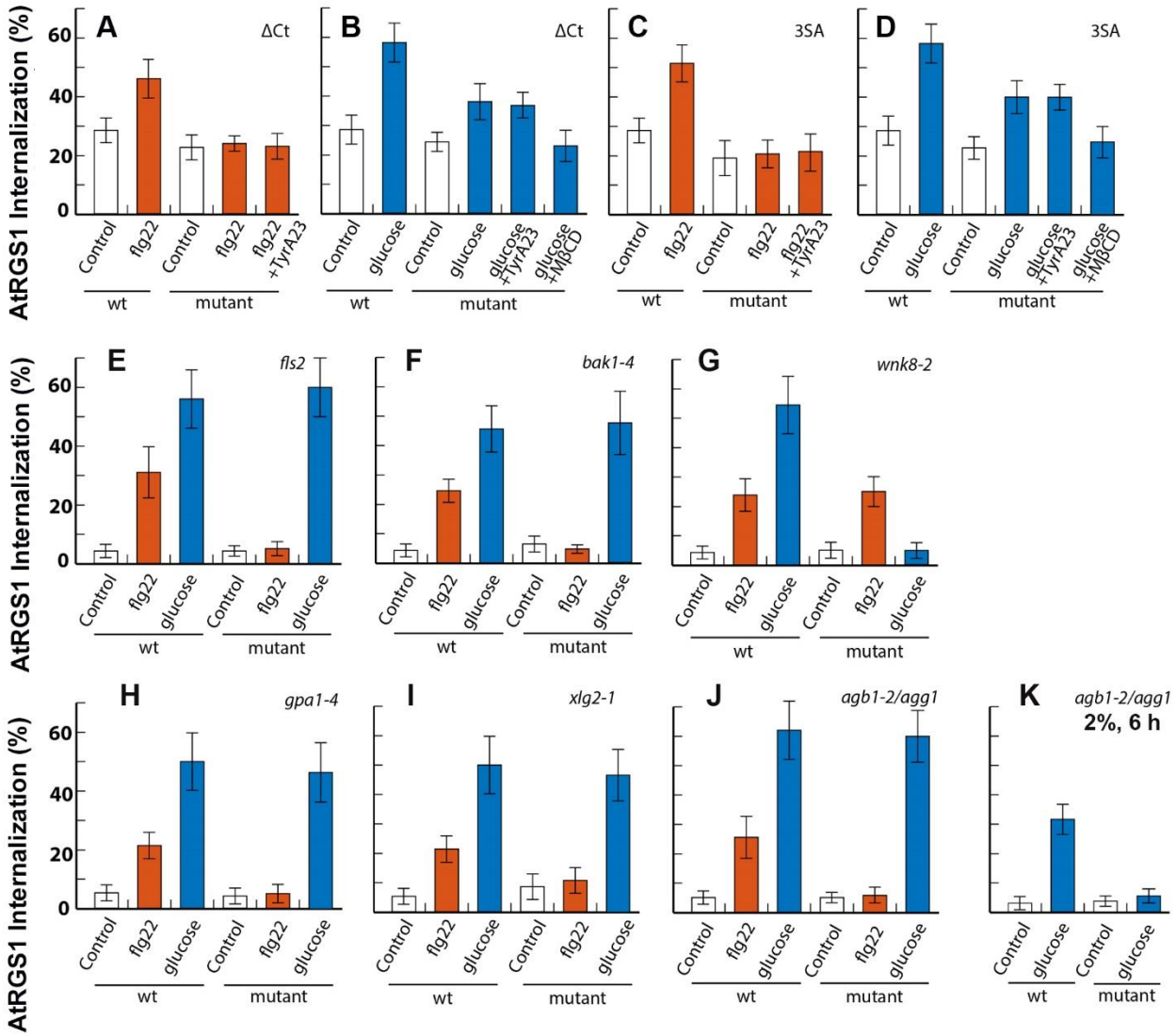

1578 Figure 4
1579

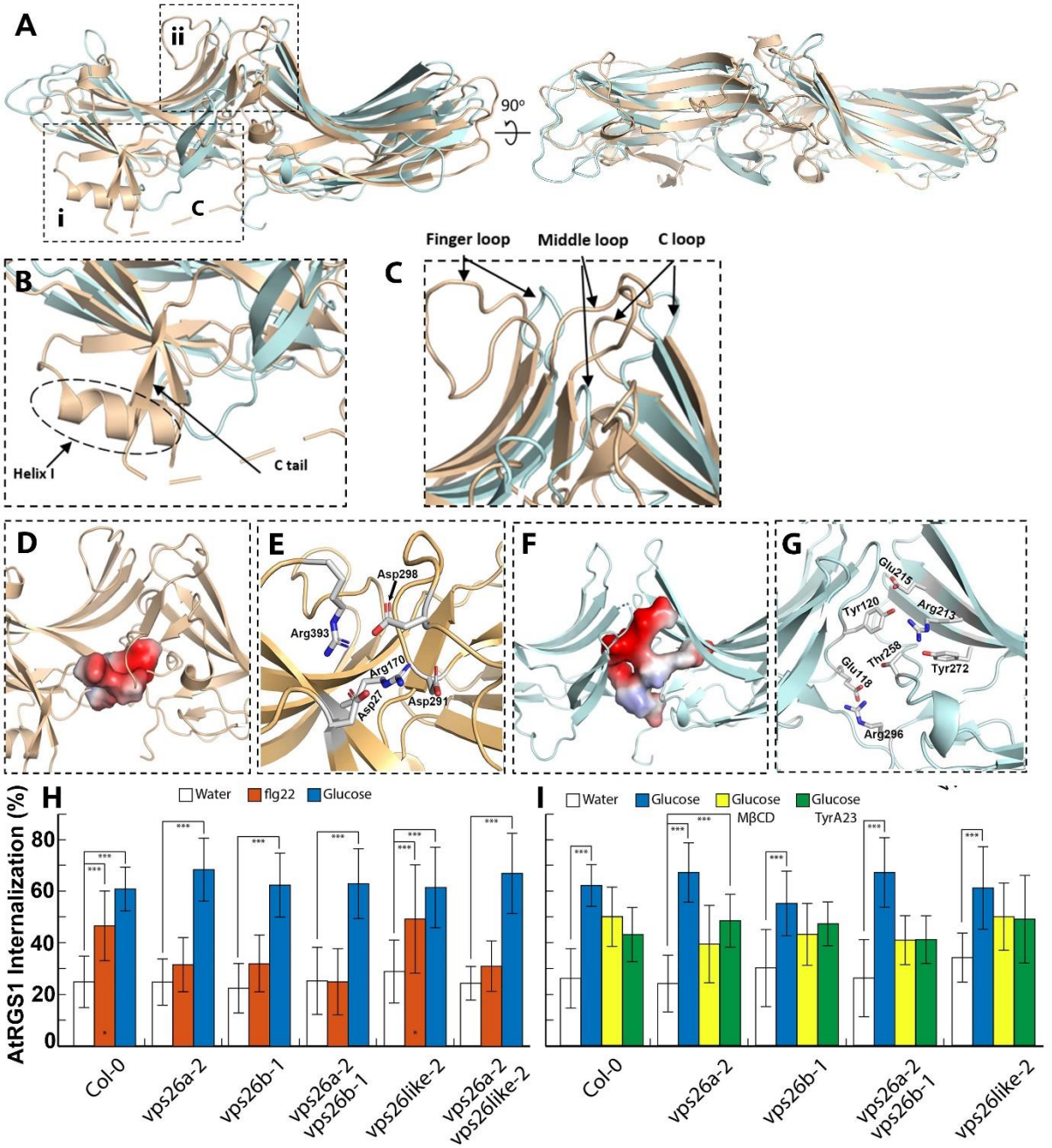

1580
1581
1582
1583
1584
1585
1586
1587

Figure 5

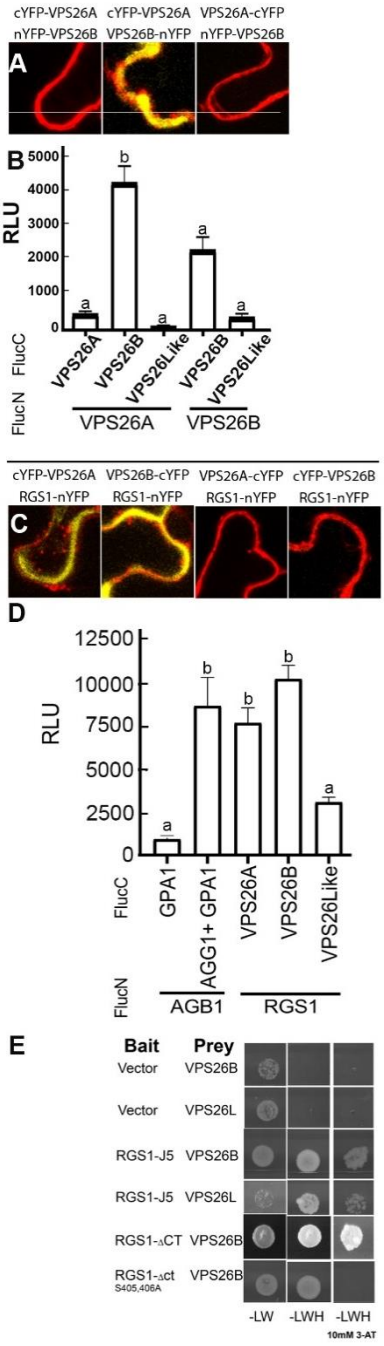

Figure 6

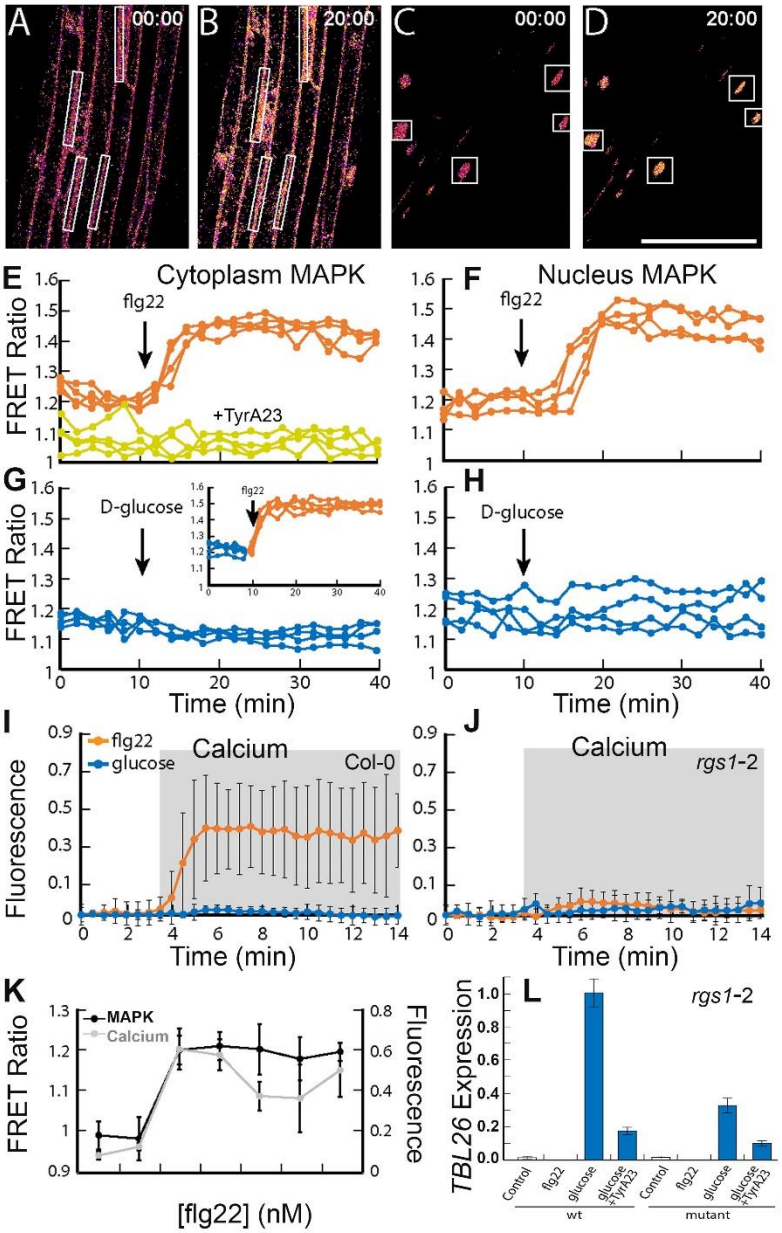

1611 Figure 7

1612

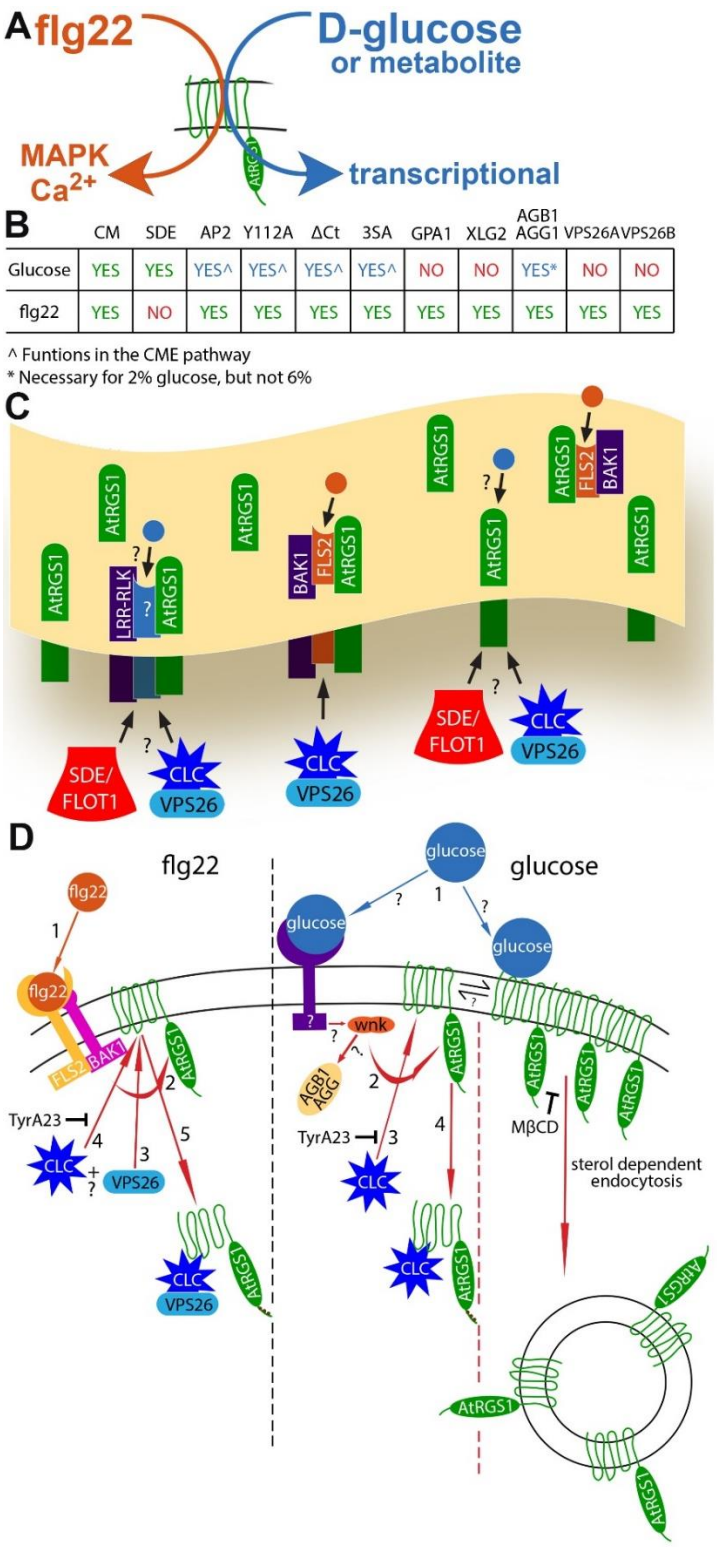

B

	CM	SDE	AP2	Y112A	ΔCt	3SA	GPA1	XLG2	AGB1 AGG1	VPS26A	VPS26B
Glucose	YES	YES	YES^	YES^	YES^	YES^	NO	NO	YES*	NO	NO
flg22	YES	NO	YES	YES	YES	YES	YES	YES	YES	YES	YES

^ Funtions in the CME pathway
* Necessary for 2% glucose, but not 6%

1613
1614

Figure S1

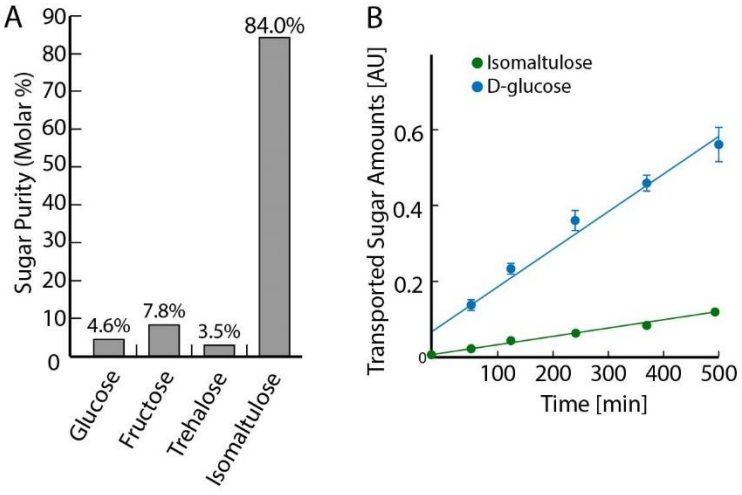

Figure S2

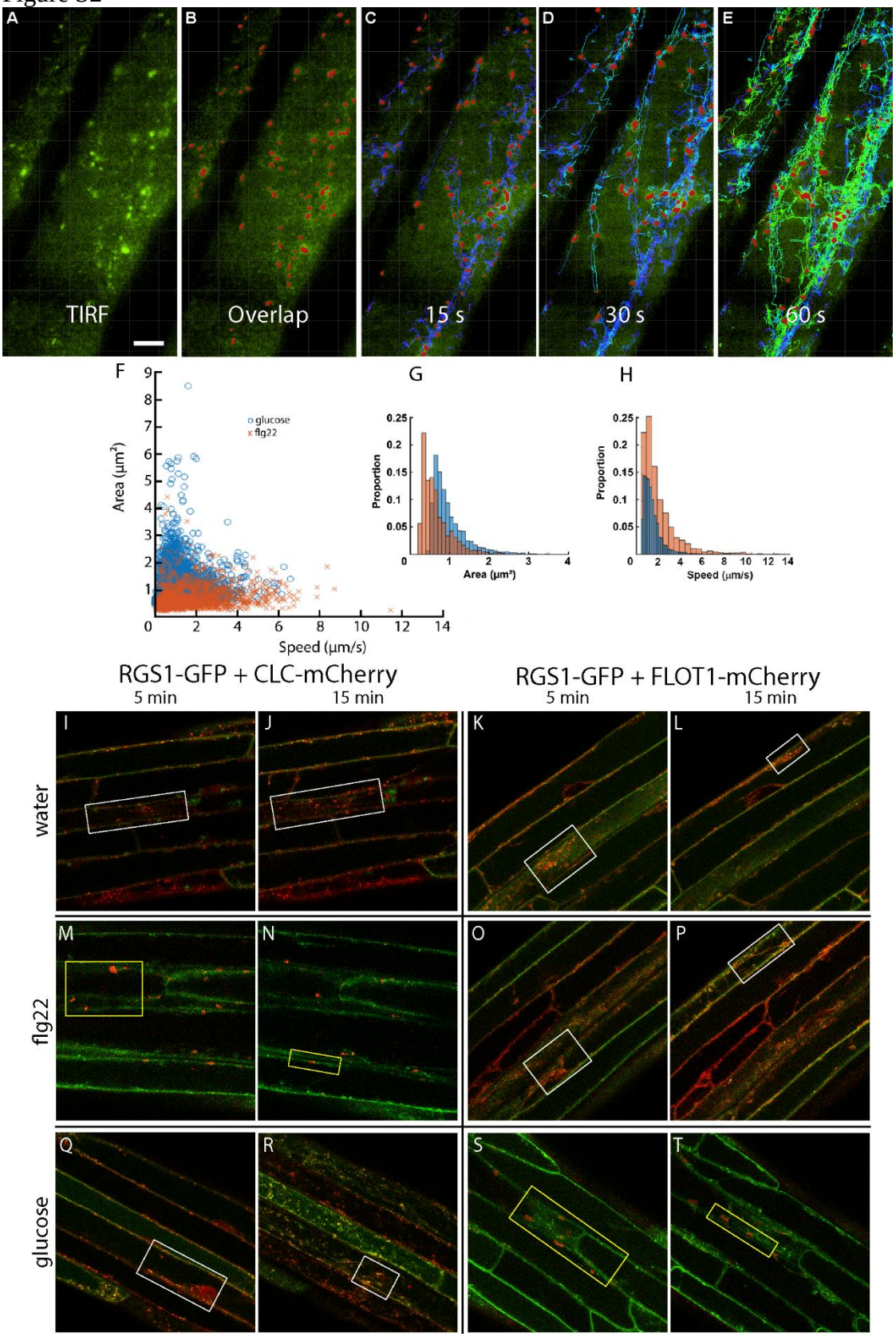

Figure S3

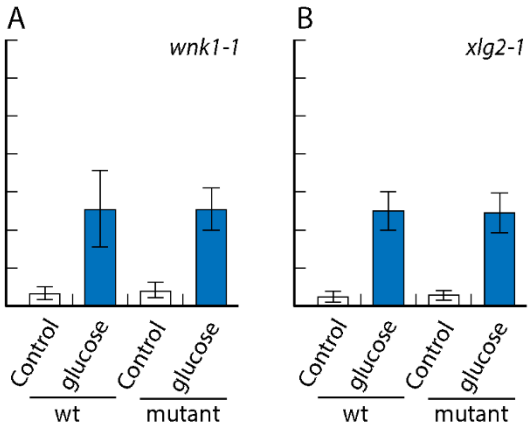

Figure S4

A

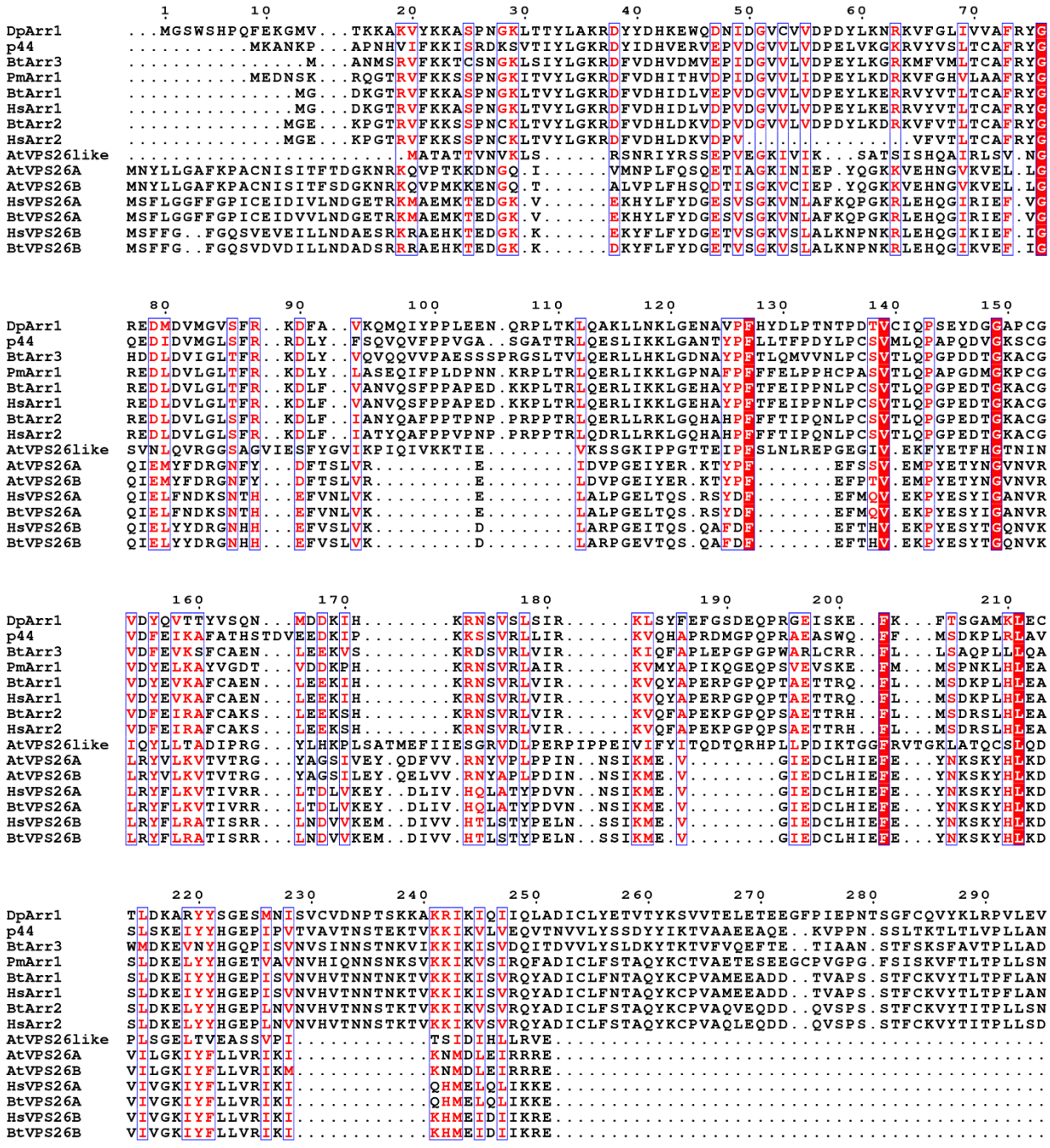

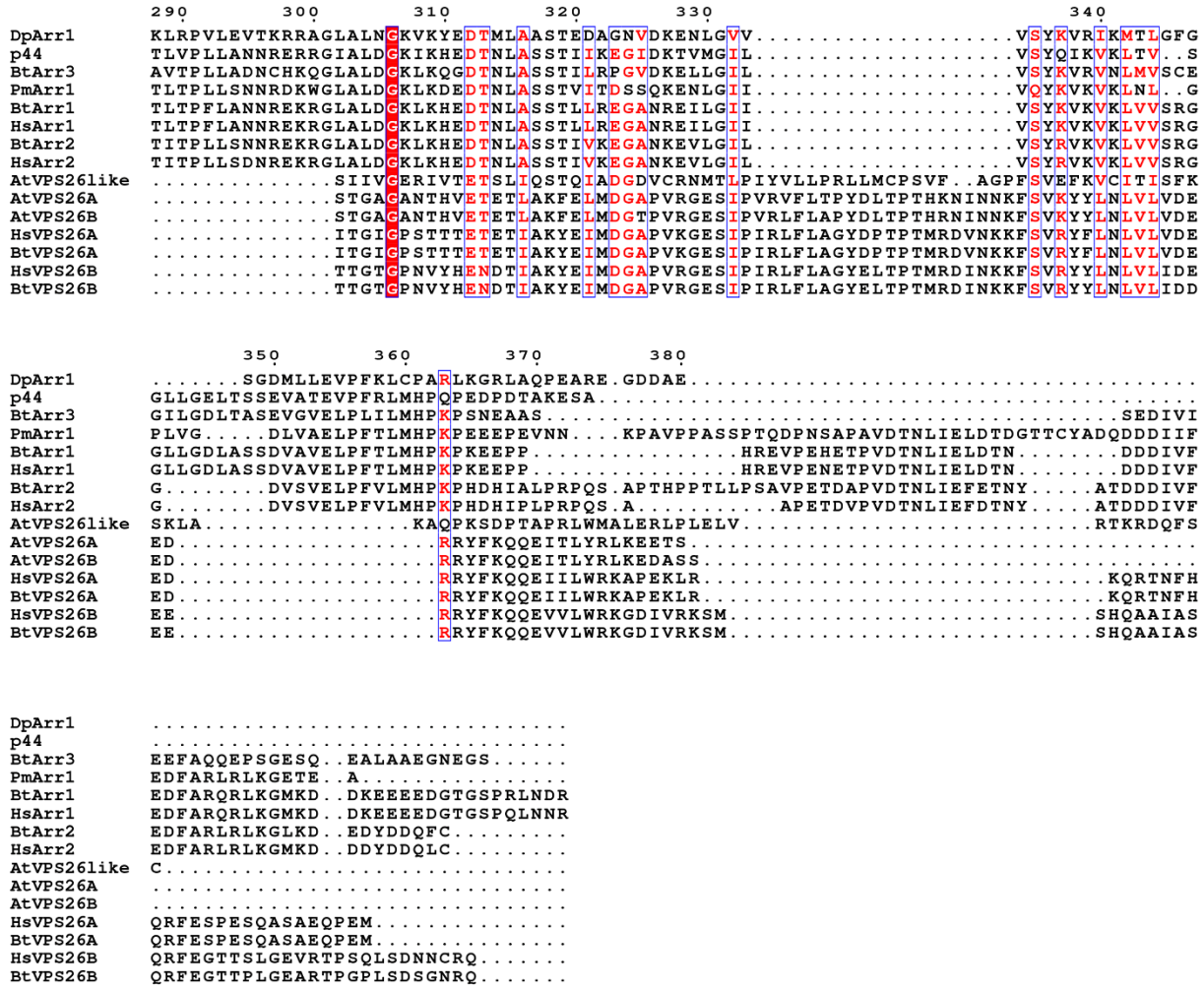

B.

1: DpArr1	100.00	37.22	38.42	46.98	46.61	46.89	43.13	42.03	19.03	18.22	19.77	15.44	15.44	16.73	16.73
2: p44		100.00	52.79	49.72	59.50	59.22	56.46	56.01	18.56	15.16	15.16	12.65	12.65	12.24	12.65
3: BtArr3			100.00	50.00	60.77	60.51	56.58	54.79	17.10	16.03	16.03	13.51	13.51	14.61	16.10
4: PmArr1				100.00	66.33	66.58	63.48	63.09	17.86	17.41	18.55	12.96	12.96	14.65	15.02
5: BtArr1					100.00	99.04	77.81	78.33	17.54	19.83	19.83	14.67	14.67	15.36	16.10
6: HsArr1						100.00	78.05	78.59	17.16	19.41	20.25	14.29	14.29	14.98	15.73
7: BtArr2							100.00	96.95	17.02	14.11	14.86	12.50	12.50	13.88	14.23
8: HsArr2								100.00	16.79	13.91	14.35	11.51	11.51	13.90	14.29
9: AtVPS26like									100.00	21.61	19.71	21.35	21.35	20.42	20.07
10: AtVPS26A										100.00	91.06	56.48	56.15	54.18	53.51
11: AtVPS26B											100.00	57.95	57.62	55.00	54.33
12: HsVPS26A												100.00	99.69	70.46	68.92
13: BtVPS26A													100.00	70.15	68.62
14: HsVPS26B														100.00	95.54
15: BtVPS26B															100.00

C.

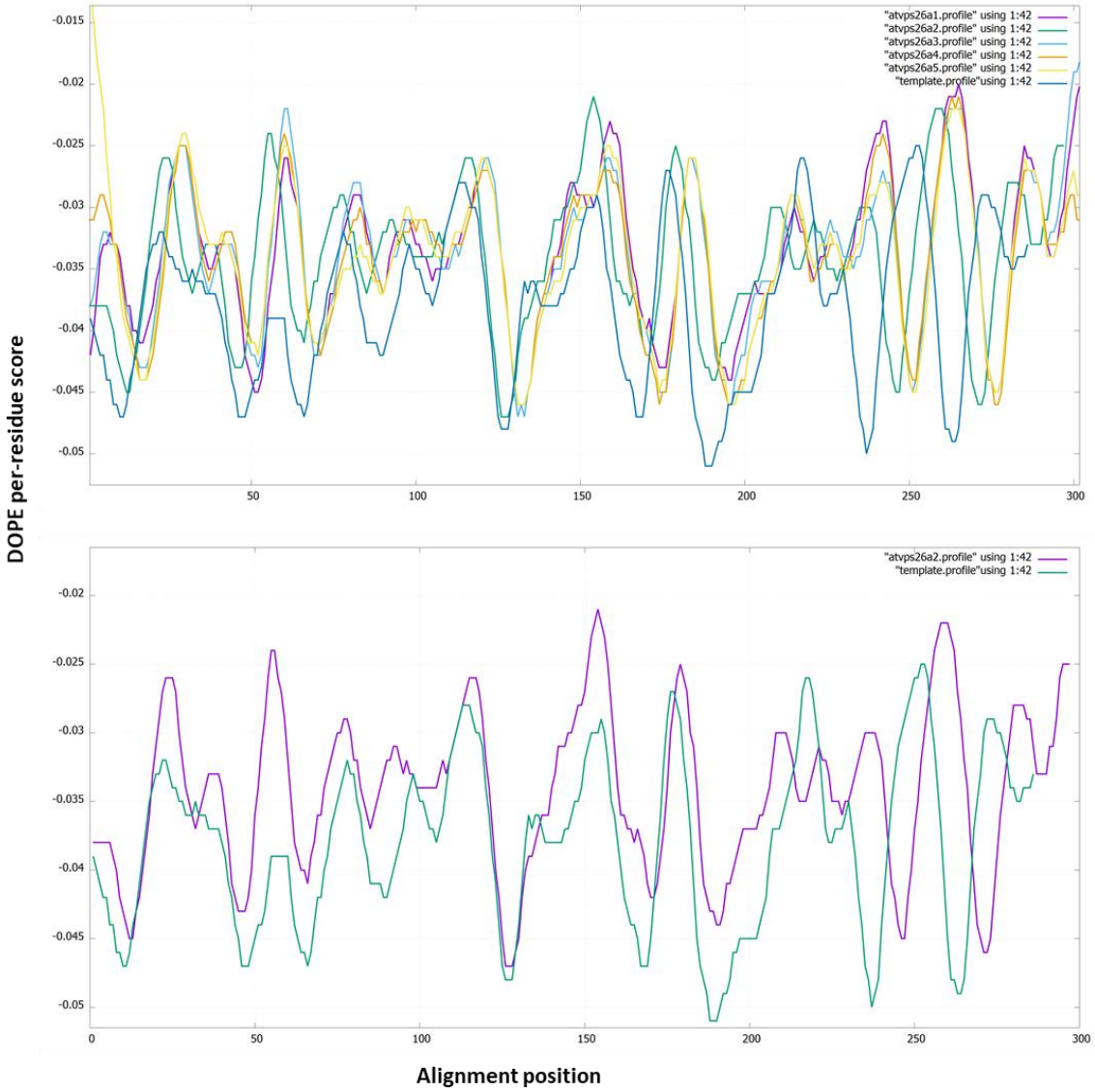

1703 D.

Filename	molpdf	DOPE score	GA341 score	RMSD
atvps26a1.pdb	2292.41699	-30278.39648	1.00000	0.309
atvps26a2.pdb	2233.81055	-30840.71289	1.00000	0.17
atvps26a3.pdb	2258.48999	-30400.76953	1.00000	0.277
atvps26a4.pdb	2212.42798	-30568.29883	1.00000	0.244
atvps26a5.pdb	2188.86987	-30466.78711	1.00000	0.217

1704

1705 E.

1706

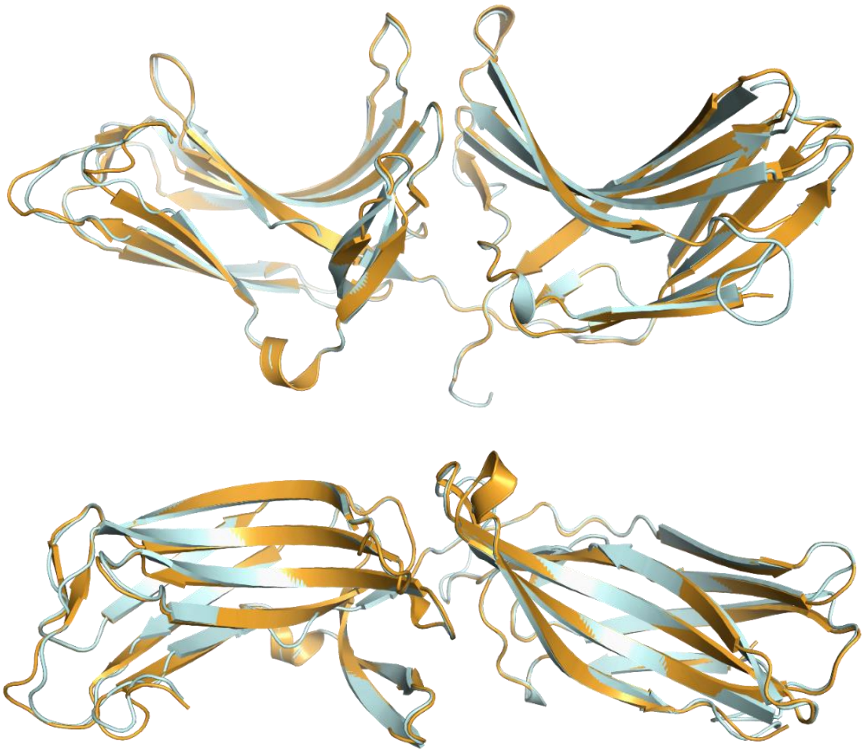

1707

1708

1709 F.

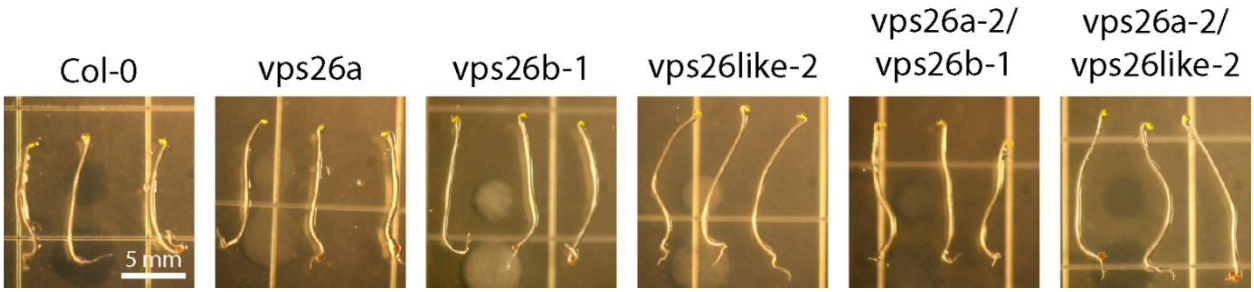

1710

Figure S5

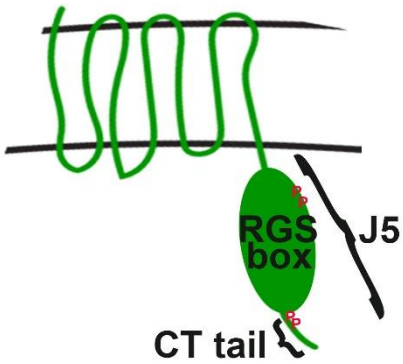

Figure S6

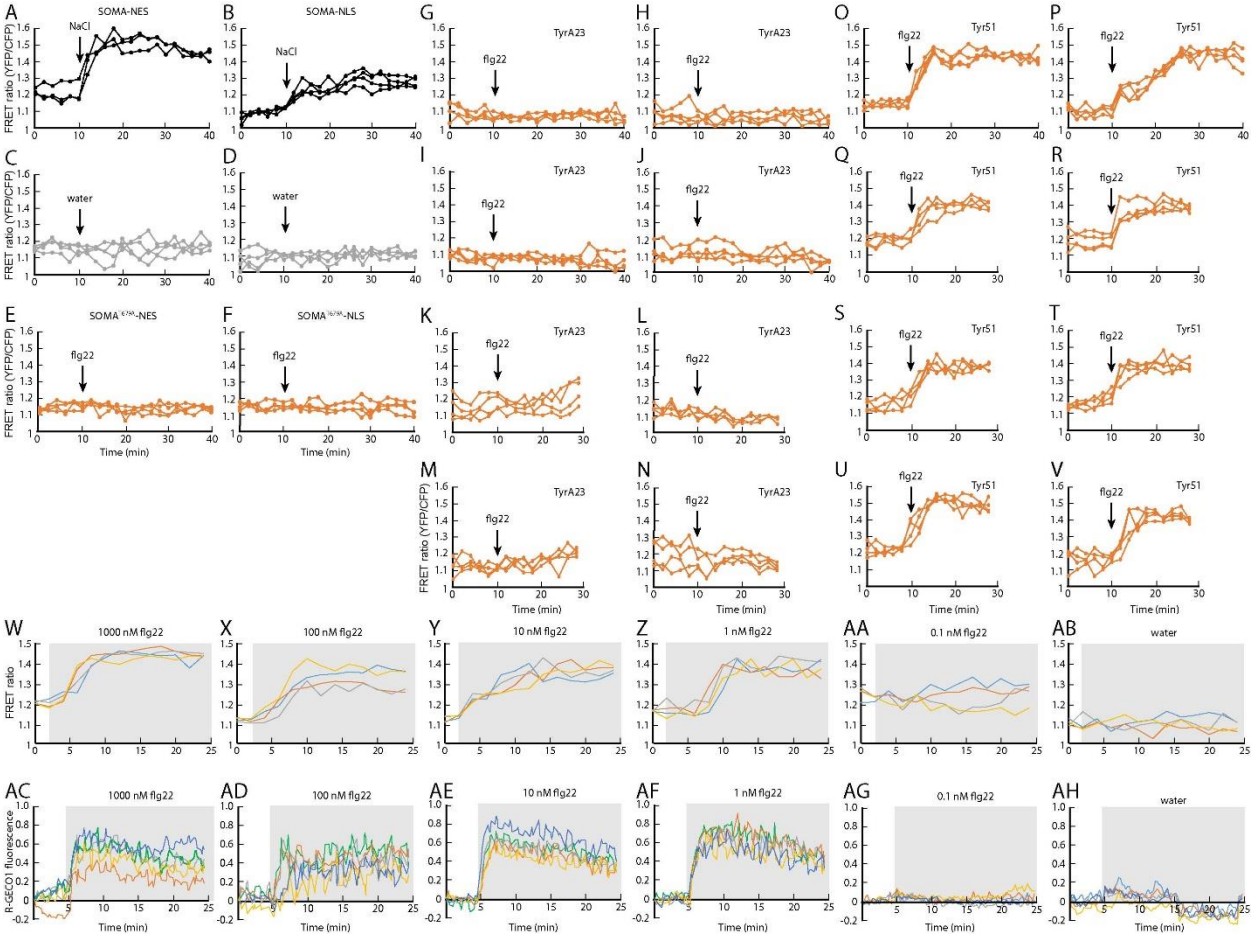

Supplemental code.

```
Data = xlsread('IMARIS statistics output')
% first step: sort the data based on the track ID, and
% subsort it on time points.
sortedData=sortrows(Data,[3,4]);
trackIDs=sortedData(:,3);
%trackIDs is only the ith column from the original sorted data, separate
%array
uniquetrackIDs=unique(trackIDs);
%uniquetrackIDs is a separate array with only unique track IDs

%StartEnd=zeros(length(uniquetrackIDs),2);
meanSpeedArea=zeros(length(uniquetrackIDs),2);

% Make a matrix with all its elements zeros. One dimension of the matrix
% is length of unique track IDs, i.e., the number of unique track IDs.
% Another dimension is 2 because we want to store the start and end
% locations of each of the unique track IDs.
for i = 1:length(uniquetrackIDs)
    ItrackID=uniquetrackIDs(i);
    locations=find(trackIDs==ItrackID);
    startLoc=locations(1);
    endLoc=locations(end);
    SpeedColumn=sortedData(:,1);
    meanSpeedArea(i,1)=mean(SpeedColumn(startLoc:endLoc));
    AreaColumn=sortedData(:,2);
    meanSpeedArea(i,2)=mean(AreaColumn(startLoc:endLoc));
    %StartEnd(i,1)=startLoc;
    %StartEnd(i,2)=endLoc;

end
```